博士論文

Pharmacokinetic characterization and therapeutic efficacy of halofuginone micelle nanoparticles in murine models of Nrf2 activated lung adenocarcinoma

(Nrf2 活性化肺腺癌マウスモデルにおけるハロフギノンミセルナノ粒子の薬物動態および有効性の検討)

東北大学大学院医学系研究科医科学専攻
生体機能学講座医化学分野
Harit Panda

Contents

Abstract

The Keap1-Nrf2 system is the master regulator of the cellular response against oxidative and xenobiotic stresses. Constitutive activation of Nrf2 is frequently observed in various types of cancers. Nrf2 hyperactivation induces metabolic reprogramming in cancer cells, which supports the increased energy demand required for rapid proliferation and confers high-level resistance against anticancer radio/chemotherapy. Hence, Nrf2 inhibition has emerged as an attractive therapeutic strategy to counter such acquired resistance in Nrf2-activated tumors. My laboratory previously identified Halofuginone (HF) as a promising Nrf2 inhibitor. In this study, I pursued preclinical characterization of HF and found that while HF markedly reduced the viability of cancer cells, it also caused severe hematopoietic and immune cell suppression in a dose-dependent manner. Hence, to overcome this toxicity, I decided to employ a nanomedicine approach to HF. We found that encapsulation of HF into a polymeric micelle (HF micelle; HFm) largely relieved the systemic toxicity exhibited by free HF while maintaining the tumor-suppressive properties of HF. LC-MS/MS analysis revealed that the reduction in the magnitude of adverse effects was the result of the ability to release HF from the HFm core in a slow and sustained manner. These results thus support the contention that HFm will potentially counteract Nrf2-activated cancers in the clinical settings.

1. Introduction

The Kelch-like ECH-associated protein 1 (Keap1)-NF-E2-related factor 2 (Nrf2) system is acknowledged to be one of the major contributors to cellular defense against oxidative and xenobiotic stresses triggered by either endogenous or exogenous insults (1). Keap1 is a cysteine thiol-enriched adaptor protein that acts as a stress sensor for the transcription factor Nrf2 by connecting Nrf2 and Cullin-3 (Cul3), forming a ubiquitin E3 ligase complex (2). In the cytoplasm under quiescent conditions, Nrf2 is polyubiquitinated by the Keap1-Cul3 ubiquitin E3 ligase complex, leading to its rapid proteasome-dependent degradation. In contrast, cellular insults, such as exposure to electrophilic stress, inactivate the E3 ligase function of Keap1, permitting Nrf2 to escape proteasomal degradation (Fig 1). In the nucleus, Nrf2 forms a heterodimer with one of the small MAF proteins (sMAFs) and binds to the antioxidant-responsive element (ARE) or CNC-sMAF binding elements (CsMBEs) motif (3-6) or resulting in robust activation of a battery of cytoprotective genes. The canonical Nrf2 target genes include NADPH:quinone oxidoreductase 1 (encoded by *Nqo1*), the glutamate cysteine ligase catalytic and modifier subunits (*Gclc* and *Gclm*), and reactive oxygen species (ROS)-eliminating antioxidant enzymes, including heme oxygenase 1 (*Hmox1*) and peroxiredoxin 1 (*Prdx1*) (3,7,8).

The Cancer Genome Atlas (TCGA), which includes data generated using the latest sequencing analysis methods, has helped to identify a multitude of pan cancer somatic variants that exploit various signaling pathways to drive and sustain tumorigenesis (9,10). The KEAP1-NRF2 pathway is one such pathway that is frequently activated in cancer cells (10). Somatic mutations in the *KEAP1* and *NRF2* (*NFE2L2)* genes are frequently observed in different kinds of cancers. Activating mutations in the KEAP1-NRF2 axis are found in approximately 30% of

esophageal carcinomas, 34% of squamous cell lung carcinomas and 19% of hepatocellular carcinomas (11-13).

Such mutations lead to aberrant NRF2 production in tumors. Although NRF2 activation in host cells helps mitigate a plethora of chemical stresses by coordinately activating various genes encoding antioxidative stress response enzymes/proteins and phase II metabolic enzymes, constitutive NRF2 accumulation in cancer cells confers chemo/radiotherapy resistance and supports malignant growth (11,14). This constitutive NRF2 accumulation has been shown to be induced via mutually exclusive mutations in various regions of NRF2, KEAP1 or CUL3. In NRF2, the DLG and ETGE motifs of the Neh2 domain exclusively bear these somatic mutations. The Neh2 domain is in the N-terminal region of NRF2 gene and contains seven lysine residues in a centralized α-helix region, and these lysine residues are targets of ubiquitinase. The peptide motifs (DLG and ETGE) on both sides of the α-helix region of Neh2 region interact with KEAP1. Since the Neh2 domain plays an important role in binding to KEAP1 protein it invariably harbors all the somatic mutations as mentioned above as it results in stabilization and subsequent hyperactivation of NRF2.

The DLG and ETGE regions are pivotal for the KEAP1-NRF2 interaction. In the case of KEAP1 and CUL3, loss-of-function mutations are found throughout the coding region (15). Indeed, patients with these mutations have a poor prognosis and increased mortality. For example, the mean overall survival of non-small cell lung carcinoma (NSCLC) patients with aberrant NRF2 production is as low as 11.2 months, while that of those lacking this alteration is 36.8 months. NRF2-activating mutations are more pertinent in the context of lung tumors, as 30% of all NSCLCs have mutations in KEAP1, and 20% of all KRAS-driven lung adenocarcinomas (LUADs) have

KEAP1 or NRF2 co-mutations. Hence, I used the $Keap1^{FB/FB}$::$Kras^{G12D}$ lung adenocarcinoma model system in the current study, as it has high clinical relevance.

Furthermore, because of the lack of approved therapies for NRF2-activated cancers, there is an important unmet clinical need to find a viable therapy to treat patients with such tumors. Given the above findings and reports, it was hypothesized that using NRF2 inhibitors would be a reasonable approach to tackle such NRF2-addicted/activated cancers. To this end, using a luciferase (Luc) assay-based high-throughput screening of the Tohoku University School of Pharmaceutical science chemical library, my laboratory identified halofuginone (HF;) as a potent NRF2 inhibitor (16) and provided preclinical proof-of-concept evidence of its role as an anticancer chemosensitizer using xenograft murine models of NRF2-activated cancer. The decrease in NRF2 accumulation induced by HF was mediated through an amino acid starvation response. HF inhibits prolyl-tRNA synthetase (PRS), which results in the accumulation of uncharged tRNAs in cells (16). This leads to an amino acid starvation response and global suppression of protein translation via the GCN2-eIF2 pathway. HF use successfully regressed NRF2-activated tumors in our earlier experiments, but my laboratory also observed toxicity in mice when HF was used in combination with cisplatin, as the mice exhibited a significant decrease in body weight (16). Since these experiments were carried out in nude mice bearing a KYSE70 (Nrf2 addicted esophageal squamous carcinoma cells) xenograft, which lack T-cell immunity, I decided to use a much more sophisticated model system for our current project. Hence, I decided to use the $Keap1^{FB/FB}$::$Kras^{G12D}$ murine model, which resembles Kras-driven Nrf2-activated lung adenocarcinoma, in my current study.

Moreover, my laboratories' earlier studies suggest that although Nrf2 inhibition in tumors seems to be a plausible approach to treat Nrf2-activated cancers, Nrf2 activation in host immune

cells has also been shown to suppress tumor progression and metastasis (17-20). Hence, tumor-specific inhibition of Nrf2 would result in better tumor suppression. To achieve tumor specificity and induce a therapeutic response devoid of any adverse effects, I hypothesized delivering HF as a nanomedicine to passively target Nrf2-activated cancers. The development of the nanomedicine reduced HF accumulation in healthy organs in my experiments, decreasing the chances of side effects and consequently increasing the therapeutic window of HF (Fig 2). Recently, polymeric micelles have received considerable attention as a potent nanomedicine for the specific targeting of tumor cells (21,22). These nanomedicines work on the widely accepted principle of the enhanced permeability and retention (EPR) effect (21,23) of solid tumor models, which is characterized by hyperpermeability of the microvasculature to circulating macromolecules and compromised lymphatic drainage (23,24). Because of the aberrant growth of the tumor cells, the endothelial linings of the adjoining blood vessels develop gaps, this makes any drug to easily access the tumor tissue. Once a drug enters the tumor, because of the decline in the lymphatic activity in the tumor area it becomes difficult for the drug to exit it. This forms the basis of the EPR effect.

Using a polymeric micelle system ensures prolonged circulation of the polymer-drug complex in the bloodstream (25). Since the drug is released slowly from the core of the complex in the blood vessel, it has more time to accumulate in the tumor tissue avoiding normal healthy organs due to aforementioned EPR effect. It is important to mention here that some polymeric micelles incorporating drugs are already in clinical use (26).

In the current study, my collaborators developed a novel polymeric micelle incorporating HF via an ester bond between HF and poly(ethylene glycol)-poly(aspartic acid) [PEG-PAsp] block copolymers (HFm) and I evaluated its efficacy in eliminating Nrf2-activated lung adenocarcinoma

in a murine model. I found that while both HF and HFm (Fig 3A and B) significantly regressed Nrf2-activated lung tumors in mice, HFm treatment completely rescued the acute systemic toxicity caused by free HF administration. These results unequivocally demonstrate that HFm is a potent Nrf2 inhibitor without any apparent toxicity and can potentially play a significant role in clinical settings in the future.

2. Materials and Methods

2.1. Reagents

Halofuginone hydrobromide (HF, CAS 64924-67-0) was purchased from Carbosynth Limited (code no. FH23731, Berkshire, UK). An HF stock was prepared using dimethyl sulfoxide (DMSO) at a concentration of 10 mg/mL. The stock solution was further diluted with saline. α-Methoxy-ω-aminopropyl poly(ethylene glycol) (PEG-NH_2) with a molecular weight of 12 kDa was purchased from NOF CORPORATION (Tokyo, Japan). β-Benzyl-L-aspartate *N*-carboxy-anhydride (BLA-NCA) was purchased from Chuo Kaseihin Co., Inc. (Tokyo, Japan).

2.2. Synthesis of HF-modified PEG-PAsp (PEG-PAsp(HF))

Poly(ethylene glycol)-poly(β-benzyl-L-aspartate) (PEG-PBLA) was synthesized by ring-opening polymerization of BLA-NCA using PEG-NH_2 (NOF Corporation, Tokyo) as a macroinitiator, as previously reported (27). For this study, 500 mg of PEG-NH_2 and 456 mg of BLA-NCA (Chuo Kaseihin Co., Inc., Tokyo) were used for PEG-PBLA polymerization. The degree of polymerization of PBLA segment in PEG-PBLA was determined to be 40 from ^{1}H nuclear magnetic resonance (NMR) spectra (solvent: DMSO-*d6*, temperature: 80°C) (JNM-ECS 400, JEOL Ltd., Tokyo). PEG-PBLA was dissolved in 0.5 M NaOH aq. (5 equivalents to BLA) for 1 hour at room temperature for deprotection. The reaction mixture was then poured into a dialysis membrane (MWCO: 12–14 kDa) and dialyzed against 0.01 M HCl aq. for a half day and deionized water for a half day, followed by lyophilization. The obtained PEG-PAsp was dissolved in *N*,*N*-dimethylformamide (10 mg/mL). 2-Methyl-6-nitrobenzoic anhydride (1.2 equivalents to Asp) and 2,2-dimethoxypropane (1.5 equivalents to Asp) were mixed with the PEG-PAsp solution and stirred for 20 min at 25°C. HF was separately dissolved in DMF (1.0 equivalent to Asp, 6 mg/mL)

and added to the PEG-PAsp solution. The mixture was stirred for 1 day protected from light. The mixture was poured into a dialysis membrane (MWCO: 6–8 kDa) and dialyzed against deionized water for 2 days for micelle formation protected from light. The dialyzed solution was passed through a 0.45-μm syringe filter and concentrated by ultrafiltration (MWCO: 30000), followed by further filtration with a 0.22-μm membrane for sterilization.

The diameter and size distribution (polydispersity index) of the obtained PEG-PAsp(HF) micelles were determined to be 38 nm and 0.12, respectively, by dynamic light scattering using a Zetasizer Nano equipped with a He–Ne laser (Malvern Instruments, Worcestershire, UK). One milliliter of micelle solution was sampled and lyophilized to adjust the micelle concentration and calculate the amount of loaded HF. The weight of the dried powder was measured, and then the powder was dissolved in DMSO-*d6* with 2% D2O and 0.05% TMS, followed by ^{1}H NMR measurement (temperature: 80°C). The amount of loaded HF was determined to be 14.4 per polymer from the peak intensity ratio of PEG protons (1090 H) to the benzyl protons of HF (43.2 H). The PEG-PAsp(HF) micelle solution was stored at –80°C until use.

PEG-PAsp(HF) was synthesized by my supervisor's collaborators Prof. Kanjiro Miyata and Dr. Mitsuru Naito of University of Tokyo. I am grateful to them for their constant support throughout the course of this study.

2.3. Cell culture

WT-GFP and Keap1-mCherry Hepa1 cells were prepared as described previously (28). These cells were maintained in Dulbecco's modified Eagle's medium (DMEM) supplemented with 10% (v/v) fetal bovine serum and antibiotics (penicillin–streptomycin) at 37 °C with 5% CO_2. I would like

to thank Dr. Liam Baird for providing me the WT-GFP and Keap1-mCherry Hepa1 cell lines for the current project.

2.4. Cell fluorescence analysis

For cell viability analysis, 4 x 10^4 WT-GFP cells and 2 x 10^4 Keap1 mCherry Heap1 cells were cultured separately on day –1 in black 96-well plates (Corning; number 3904). On day 0, HF or saline was introduced at different concentrations, and the plates were then returned to the 37°C incubator until day 2. Cell viability was determined by measuring the fluorescence intensities of the cells using a PHERAstar FS microplate reader (BMG Labtech, Ortenberg, Germany).

2.5. Immunoblotting

For analyses of cultured cells, 1 x 10^6 WT-GFP and Keap1-mCherry Hepa1 cells were seeded separately on day –1 and treated with 50 nM HF the following day (day 0). Whole-cell lysates were prepared by lysing the cells in SDS buffer (0.25 M Tris-HCl (pH 6.8), 8% (w/v) SDS and 20% glycerol) and collected at 0, 3-, 6-, 12- and 18-hours following HF treatment. An anti-Nrf2 antibody (Cell Signaling Technology, #12721, 1:500 dilution) and anti-α-tubulin antibody (Sigma, T9026, 1:1000 dilution) were used.

2.6. Mice

The generation of $Keap1^{FB/FB}$::$Kras^{G12D}$ mice was performed as described previously (20,29,30). The $Keap1^{FB/FB}$ mice here refers to the Keap1-knock down mice with deletion of 3,4 and 5 exons of the Keap1 gene (this deletion is mediated by the Cre-Lox recombination. $Kras^{G12D}$ is a widely used cancer model mice with activation of Kras oncogene (with G12D mutation; Glycine replaced

by Aspartic acid at 12 position). All mice used in this study were on the C57BL/6J background. Saline, HF and HFm were administered intravenously to the mice in this study because polymeric micelles are known to more stable when injected into the blood stream directly.

All *in vivo* experiments were approved by the "The Institutional Animal Care and Use Committee" of the "Tohoku University Environmental & Safety Committee".

2.7. Intranasal administration of an adenovirus expressing Cre recombinase (Adeno-Cre)

Adeno-Cre was purchased from VectorBioLabs (Ad-Cre-GFP, catalog no. 1700). Intranasal Adeno-Cre administration was performed as described previously (31). Briefly, 1×10^7 plaque-forming units of Adeno-Cre were mixed with Eagle's minimum essential medium (MEM) and calcium chloride. The mixture was incubated for 20 min on ice and used for intranasal instillation within 1 hour of preparation. Droplets containing the Adeno-Cre mixture were administered to the nostrils of anesthetized mice (8–12 weeks old) with a pipette. The mice were allowed to gradually inhale the droplets.

2.8. Flow cytometry

Mononuclear cells were isolated from the bone marrow, spleen and thymus using Ficoll-Paque PREMIUM 1.084 (Cytiva 17-5446-02). The mononuclear cells were stained with allophycocyanin-eFluor 780-conjugated anti-c-Kit (Invitrogen; Clone 2B8), Brilliant Violet 510-conjugated anti-B220 (Biolegend; Clone RA2-6B2), phycoerythrin-conjugated anti-F4/80 (Biolegend; Clone BM8), fluorescein isothiocyanate-conjugated anti-Ly6G (Biolegend; Clone 1A8), Brilliant Violet 421-conjugated anti-CD11b (Biolegend; Clone M1/70), fluorescein isothiocyanate-conjugated anti-CD71 (eBiosciences; Clone R17217), phycoerythrin-conjugated

anti-Ter119 (eBiosciences; Clone TER-119), PE-Cyanine7-conjugated anti-CD4 (Invitrogen; Clone GK1.5) and allophycocyanin-conjugated anti-CD8 (Biolegend; Clone S3-6.7). Propidium iodide staining was used to remove dead cells. Analyses were performed using a FACSVerse (BD Biosciences). Data were analyzed using FlowJo software (BD Biosciences).

2.9. Liquid chromatography–tandem mass spectrometry (LC-MS/MS) analysis

HF was quantified following the method published by Matus *et al*. (32) with slight modification. Briefly, approximately 30 mg of frozen tissue was placed in a 2-mL plastic tube, and 600 μL of acetonitrile/2-isopropanol (3:2, v/v), 15 mg of anhydrous sodium acetate, and 10 mg of anhydrous magnesium sulfate were added. For the internal standard, HF-13C6 HBr (Honeywell/Fluka, Germany) was used. Samples were vigorously mixed for 50 sec, homogenized in an ultrasonic bath for 10 min and then shaken for 30 min. The mixtures were centrifuged at 16000 x g for 10 min. The supernatants were diluted with an equal volume of water and centrifuged at 16000 x g for 10 min. Thirty microliters of supernatant was injected into an ultrahigh performance liquid chromatography (UHPLC)-MS/MS system.

UHPLC-MS/MS analysis was performed on an Acquity Ultra Performance LC I-class system equipped with a binary solvent manager, a sample manager, and a column heater (Waters) interfaced with a Waters Xevo TQ-S MS/MS system equipped with electrospray ionization operated in the positive-ion mode. MS/MS was performed using the multiple reaction monitoring mode. The capillary voltage was 3.5 kV, and the cone voltage was 120 V. The source offset and temperature were set at 50 V and 150°C, respectively, with a cone gas flow rate of 150 L/h. The desolvation temperature was set to 500°C, and the desolvation gas flow, collision gas flow and nebulization gas flow were set to 1000 L/h, 0.15 ml/min and 7.00 x 10^5 Pa, respectively. Both the

cone and nebulization gases were nitrogen. LC separation was performed using a reversed-phase column (Acquity UPLC BEH C18; 100 mm by 2.1 mm [inner diameter], 1.7-µm particle size; Waters Corp.) with gradient elution of solvent A (0.1% formic acid/water, v/v) and solvent B (100% acetonitrile) at 0.5 ml/min. The initial condition was set to 5% solvent B and maintained for 1 min. Solvent B was increased linearly to 95% over 4 min, and this condition was maintained for 2 min. Finally, the mobile phase was returned to the initial conditions, which were maintained for 2 min until the end of the run. The column oven temperature was 50°C. Data were collected using MassLynx v4.1 software (Waters) and analyzed using Traverse MS v1.2.7 software (Reifycs).

All the LC-MS/MS experiments were carried out by Mrs. Ritsumi Saito of the Medical Biochemistry department. I would like to acknowledge the help provided by her for conducting these experiments which were pivotal to this study.

2.10. Hematological analysis

Hematological indices were measured using an automatic blood cell analyzer (Nihon Kohden).

2.11. Histology

Lung tissues were fixed with 10% formalin (Mildform 10N; FUJIFILM Wako, Osaka) and embedded in paraffin. Sections were stained with hematoxylin-eosin (HE) or Elastica-Masson (EM). To measure the tumor area, 5 sections were cut at regular intervals and stained with HE. The tumor area was measured using ImageJ software (NIH).

2.12 RNA extraction and reverse transcription polymerase chain reaction

Total RNA was extracted with Sepazol RNA I Super G reagent (Nacalai Tesque) and reverse-transcribed with a ReverTra Ace qPCR RT Kit (Toyobo) according to the manufacturer's instructions. The resulting cDNA was used as a template for quantitative reverse transcription polymerase chain reaction (RT-qPCR) using TaqMan with a QuantStudio 6 Real-Time PCR Analyser (Thermo Fisher Scientific). The abundance of mRNA levels was normalized to *rRNA* abundance.

3. Results

3.1. HF targets Nrf2-activated cancer cells by suppressing Nrf2 accumulation *in vitro*

HF has been reported to suppress Nrf2 accumulation within cells (16). To investigate the tumor-suppressive role played by HF in Nrf2-activated tumor cells, I treated wild-type (WT) Hepa1 cells expressing enhanced green fluorescent protein (EGFP) (WT-GFP) and Keap1 knockout cells expressing mCherry (Keap1 KO-mCherry) with HF. Both isogenic cell lines were established previously in my laboratory (28). Keap1 is the negative regulator of Nrf2 and knocking out Keap1 causes constitutive activation of Nrf2. As shown in Figure 4A, fluorescence intensity (relative to saline treated cells) was measured 48 hours after the cells were exposed HF. The relative fluorescence intensity has been shown to correlate with cell viability in our previous publication (28). I found that treatment of Keap1 KO-mCherry cells with various doses of HF up to 50 nM markedly reduced the number of mCherry-positive Keap1 KO cells in a concentration-dependent manner, while the number of GFP-positive WT cells did not decrease substantially with the incremental increases in the HF concentration (Fig 4B). Figure 4C shows representative images of mCherry-positive Keap1 KO cells and GFP-positive WT cells treated with 50 nM HF; the images reproducibly show that HF treatment reduced the number of mCherry-positive Keap1 KO cells, while the number of GFP-positive cells did not decrease substantially. These results clearly indicate that HF affects the viability of Nrf2-activated Keap1 KO Hepa1 cells more severely than that of GFP-positive WT cells. The earlier publication (16) from my laboratory had similar experiments using various Nrf2-addicted (KYSE70 esophageal squamous carcinoma cells and A549 lung carcinoma epithelial cells) and Nrf2-normal (BEAS-2B lung carcinoma epithelial cells and NCC16-P11 uterine cervical epithelial cells) cancer cell lines showing similar results. The advantage of using the current system over these is that the two cell lines used in this project are

genetically identical except the mutation in Keap1 allele, so I could exclusively check the effect of HF on the Nrf2 mutation in cancer cells.

To examine whether the selective decrease in Keap1 KO cells is elicited by the suppression of Nrf2 accumulation, I carried out immunoblot analysis of the Nrf2 protein at various time points after exposing the isogenic Hepa1 cells to HF. Notably, HF challenge led to rapid depletion of the Nrf2 protein in Keap1 KO-mCherry cells (Fig 5A). On the other hand, the Nrf2 protein was undetectable in WT-GFP Hepa1 cells at all time points. I repeated this experiment and carried out densitometric measurements of the multiple immunoblots (Fig 5B). These results demonstrate that HF severely suppresses the viability of Nrf2-activated cancer cells through the rapid depletion of the Nrf2 protein.

3.2. Dose-dependent *in vivo* toxicity assessment of HF

To determine the maximal tolerated dose (MTD) of HF, preclinical animal studies were carried out. Earlier experiments with a patient-derived xenograft mouse model were carried out with an HF dose of 0.25 mg/kg of body weight (kg bw), and this dose of HF did not show any signs of acute side effects in the mice (16). In this study, therefore, I treated WT C57BL/6 mice (aged 8-12 weeks, both sexes) with incremental doses of HF ranging from 0.25 mg/kg to 1 mg/kg (Fig 6A). I administered HF every other day for a total of 4 times through intravenous tail injections.

I found that all eight mice treated with 1 mg/kg HF exhibited signs of acute distress and were moribund after 2 injections. Furthermore, these mice displayed a significant decrease in body weight (–13.4%). Since one mouse in this dose group died after the second dose, the rest of the mice in this group were euthanized before the end of the experimental protocol on day 4 (Fig 6B). These mice were excluded from subsequent analyses.

After four intravenous injections of HF, I examined blood cell markers in the peripheral blood. We found a dose-dependent decrease in the white blood cell count after HF administration, while both the red blood cell and platelet counts remained comparable among all the groups (Fig 7). To determine whether HF had any immunosuppressive effects on different cell subpopulations, we also conducted flow cytometric analysis of spleen, thymus and bone marrow samples and found that HF caused significant dose-dependent exhaustion of different hematopoietic and immune cells. HF injection produced substantial dose-dependent declines in total splenocytes and erythroblasts (Ter119+CD71+) in the spleen (Fig 8). The decrease in erythroblasts was quite significant, and most erythroblasts disappeared after the administration of 0.75 mg/kg HF. Spleen weights were also decreased incrementally as the HF dose increased.

In the bone marrow, the numbers of total cells and progenitor cells (c-Kit+) did not change substantially, but the number of B cells (B220+) was decreased with 0.75 mg/kg HF administration (Fig 9). The administration of HF gave rise to a significant dose-dependent decrease in thymus weight (Fig 10). In the thymus, total thymic cells and CD4 single-positive (CD4+CD8–) cells were decreased, and CD8 single-positive (CD4–CD8+) cells also showed a decreasing tendency.

Interestingly, these decreases in immune and hematopoietic cell populations occurred concomitantly with the significant reductions in the tissue size of the spleen and thymus.

3.3. Pharmacokinetics and biodistribution of HF-loaded polymeric micelle (HFm)

The results thus far suggested that HF caused severe systemic toxicity in WT *in vivo* models. Therefore, I hypothesized that delivering HF as a nanomedicine to passively target tumors would be a plausible approach to address this limitation by uncoupling the side effects from the therapeutic response. Therefore, I along with my collaborators developed a new class of polymeric

micelles incorporating HF via the ester bond between HF and PEG-PAsp (HFm) (Fig 11). In ^{1}H NMR spectrum, a peak corresponding to HF was detected, which revealed that 14.4 HF molecules were encapsulated by each polymer molecule (Fig 12A, peak a). Peak "b" in the spectrum corresponds to the polymer protons (Fig 12B). The hydrodynamic diameter and size distribution (polydispersity index) of HFm was determined to be 38 nm and 0.12, respectively, by dynamic light scattering (Fig 12B). The role of size of polymeric micelle has been well described in the literature (33). It has been proven that micelles with a smaller size of around 30 nm easily penetrates the tumor compared to larger 100 nm micelles. Hence, 38 nm diameter of the newly developed HFm is the perfect size for treating Nrf2 activated cancers because it will be able to accumulate in tumors relatively easily.

To determine the pharmacokinetic properties of HFm, LC-MS/MS studies were carried out using WT C57BL/6 mice. Eight- to twelve-week-old WT mice were administered saline, HF (0.75 mg/kg bw) or HFm (0.75 mg/kg bw) once. The amount of HFm was the net weight of HF excluding the micelle weight. I followed these mice up to 144 hours after administration, and spleen, liver and lung samples were collected at different time points (Fig 12C). The determination of HF levels through LC-MS/MS analysis revealed that the levels of accumulated HF in the three tissues were lower after HFm administration than after HF administration (Fig 12D). However, by the end of the study (144 hours), the HF accumulation in both the HF and HFm groups became similar, suggesting that encapsulation of HF into a polymeric micelle leads to the slow and sustained release of HF from HFm. But it is quite possible that even after 144 hours, HF was still left in the HFm core yet to be released. Because of the limitation of the experiment, it was not possible to

determine the HF still intact in HFm. I surmised that since HF accumulates quickly in large volumes when free HF is administered, HF administration leads to high systemic toxicity.

In fact, earlier publication in the literature has shown that even at earlier time points like 3 hours very high accumulations of HF was observed in various tissues CD_2F_1 mice and Fischer 344 rats (34). This makes our case stronger that using HF with a drug delivery system is highly beneficial given how quickly it accumulates in different tissues leading to high toxicity.

3.4. HF/HFm administration inhibits the progression of Nrf2-activated tumors

To determine whether HF or HFm treatment can inhibit the progression of Nrf2-activated Adenocarcinomas, we utilized a murine model of Kras-driven lung adenocarcinoma (29). Mice with the loxP-Stop-loxP $Kras^{G12D}$ knock-in allele (Kras mice) were crossed with mice harboring the Keap1-flox allele with the loxP sites encompassing the 3rd and 4th exons ($Keap1^{FB}$) (30) to obtain $Keap1^{FB/FB}$::$Kras^{G12D}$ compound mice (20). Upon Cre recombination mediated by intranasal infection with Adeno-Cre, I achieved simultaneous Kras oncogene activation and Keap1 exon deletion. I successfully mimicked Nrf2-activated lung adenocarcinoma in mice through this manipulation.

Tumors were then allowed to grow for 17 weeks before starting HF or HFm treatment. I then intravenously administered HF or HFm every other day for a total of four inoculations. Since the MTD of HF was determined to be 0.75 mg/kg bw in our earlier WT mouse experiments (Fig 6), we decided to use 0.75 mg/kg bw HF or HFm in our tumor-bearing mouse experiments as well. On the eighth day, the mice were sacrificed, and various characteristics of lung tumors were analyzed to evaluate the efficacy of HF and HFm in altering the tumor burden (Fig 13A).

I first measured lung weights. The lung weights of both HF- and HFm-treated mice were significantly lower than those of their saline-treated counterparts (Fig 13B). Lung samples were then sectioned and stained with HE (Fig 14A, upper panels). Darkly stained areas in the HE-stained sections corresponded to tumors, and the tumor areas were markedly reduced in the lungs of mice treated with HF or HFm compared with those of saline-treated mice. Similarly, the sizes of individual tumors were reduced by HF or HFm treatment (Fig 14A, middle panels). I measured the purple/blue areas using imaging software, which revealed that the tumor area was reduced by almost half (21% in the saline-treated group to 10% in the HF-treated group) or one-third (21% to 6% in the HFm-treated group) by HF or HFm treatment, respectively (Fig 14B).

I next examined the influences of HF and HFm on tumor malignancy through EM staining of lung sections (14A, lower panels). Using images of these sections, I evaluated lung lesions following the guidelines of the 2015 World Health Organization lung cancer classification system (35). Briefly, lung tumors consist of two types of lesions: lepidic and papillary pattern lesions. Lepidic pattern lesions display *in situ* growth of cells along the alveolar wall (orange arrowheads), whereas papillary pattern lesions exhibit growth away from the alveolar wall (green arrowheads). Tumors with a high prevalence of papillary lesions are labeled as grade II tumors, and patients with predominantly papillary tumors show a poorer prognosis than patients with predominantly lepidic tumors (grade I). When the major tumor components are composed of solid sheets and lack recognizable lepidic or papillary patterns, the tumor is classified as a solid tumor (grade III).

I counted the numbers of lepidic and papillary pattern tumors in sections of the lungs of $Keap1^{FB/FB}$::$Kras^{G12D}$ compound mice treated with saline, HF or HFm. I found that all three groups of mice exhibited comparable numbers of lepidic (grade I) and papillary (grade II) pattern tumors (Fig 14C). The tumor model mice treated with either HF or HFm showed a lower frequency of

papillary pattern tumors than the saline-treated controls. In contrast, grade III solid adenocarcinomas were completely absent after HF or HFm treatment. These results unequivocally demonstrate that both HF and HFm can prevent the progression of Nrf2-activated lung cancers into higher grade solid tumors.

Earlier publication from my lab (18) showed that by 17 weeks, the $Keap1^{FB/FB}$::$Kras^{G12D}$ mice develop considerable amount of tumor in the lung. Since, in the current protocol the treatment of these tumor bearing mice started at 17 weeks, it seems HF/HFm treatment in fact actively induced cell death of the cancer cells. I speculate that co-mutation of Keap1 and Kras leads to high dependence of the cancer cells on Nrf2, and its inhibition through HF/HFm treatment leads to rapid cell death. HF also activates few Nrf2 independent pathways which is talked in detail in the discussion section.

3.5. HFm reduces systemic immunosuppressive side effects

I found that HF treatment damaged healthy tissues by not only promoting severe side effects but also causing considerable cell death and systemic immunosuppression. Since the experiments in the previous section revealed that HFm produced similar or even better efficacy in lung adenocarcinoma than HF, I next assessed the capability of HFm to overcome the systemic adverse effects of HF in tumor-bearing mice. Since the encapsulation of HF in the polymeric micelle led to the slow and sustained release of HF from HFm, I hypothesized that HFm would act as a much safer drug than HF. Therefore, I examined various adverse effect markers in tumor-bearing model mice treated with 0.75 mg/kg bw HFm and compared them with those in mice treated with the same dose of HF, as 0.75 mg/kg bw is the MTD of HF.

I first measured peripheral blood indices. While mice treated with HF showed a significant decrease in the white blood cell count, HFm-treated mice did not show such a decrease, and the white blood cell count of HFm-treated mice was similar to that of saline-treated mice (Fig 15). While the mice in the HF cohort showed signs of anemia, with decreases in red blood cell and hematocrit levels, such decreases were not observed in the mice treated with HFm (Fig 15). I next examined spleen weight and found that HF administration induced a significant reduction in spleen weight but that this reduction was not observed in the HFm-treated mice (Fig 16). When I dissociated the spleen, the number of spleen cells was decreased significantly by HF treatment but not by HFm treatment, demonstrating that the reduction in spleen weight observed in the HF-treated mice was caused by the significant decrease in the absolute number of spleen cells. Similarly, HFm did not produce an apparent decrease in erythroblasts (Ter119+CD71+) in the spleen, while this cell population was significantly decreased by HF treatment. The latter is in good agreement with the earlier experiments performed with WT mice. These results thus demonstrate that HFm significantly relieves the serious adverse effects of HF on hematopoietic lineages.

I also found that the mice treated with HF showed severe signs of thymic atrophy and that the total cell number was markedly decreased (Fig 17). This thymic atrophy was completely absent in the context of HFm administration, and the total cell number in the thymus in the HFm-treated mice was comparable to that in the mice treated with saline. To address the underlying basis for the severe reductions in thymic tissue weight and cell number, I determined the major cell types within the thymus using flow cytometry. I examined double-negative cells (CD4–CD8–), double-positive cells (CD4+CD8+), CD4 single-positive cells (CD4+CD8–), and CD8 single-positive cells (CD4–CD8+). Tumor-bearing mice treated with HF showed lower numbers of the double-

negative (CD4–CD8–), double-positive (CD4+CD8+), and CD4 single-positive (CD4+CD8–) subpopulations of immune cells. In contrast, HFm treatment did not cause such decreases in the thymus, and the cell numbers were similar to those in the mice treated with saline. CD8 single-positive cells (CD4+CD8–) also showed a tendency toward a lower frequency in the mice treated mice HF compared with the mice treated with saline or HFm. Interestingly, the reductions in cell numbers were more profound for immature cells (*i.e.,* CD4-CD8- and CD4+CD8+ cells) than for differentiated CD8 and C4 single-positive cells (Fig 17).

The numbers of total bone marrow cells were also markedly reduced by free HF administration, but this reduction was not seen following the administration of HFm (Fig 18). Through flow cytometric analysis, I found that the numbers of progenitor cells (c-Kit+), B cells (B220+), macrophages (CD11b+F4/80+) and neutrophils (CD11b+Ly6G+) were severely reduced in the HF-treated mouse bone marrow compared to the HFm- or saline-treated mouse bone marrow (Fig 18). These results demonstrate that HFm is well tolerated and induces none of the systemic adverse effects that are present after HF treatment, particularly the observed severe thymic atrophy, reductions in spleen size and splenic cell number, and decrease in the peripheral white blood cell number, which are hallmarks of systemic immunosuppression.

3.6. HFm administration leads to lower HF accumulation in nontumorous tissues

To address the reason why HFm showed reduced toxicity compared with HF, I again performed LC-MS/MS analysis and determined the HF levels in tissues. To this end, I employed the tumor-bearing model mice that were utilized in the previous subsection. Three tissues, *i.e.,* the lungs, spleen, and liver, were obtained from mice treated with either HF, HFm or saline four times and

sacrificed on day 8 (Fig 19A). The tissues were homogenized *en bloc,* and the presence of HF was examined by LC-MS/MS.

I found that the HF level in tumor-bearing lungs was considerably lower in mice treated with HFm than in mice treated with free HF (Fig 19B). By the end of the 7-day treatment protocol, the lung tumors in both HF- and HFm-treated mice were considerably smaller than those in mice evaluated before treatment with these drugs. Because of the EPR effect displayed by polymeric micelles, HFm could not be incorporated efficiently into normal lung tissue (40.5 ng/g of tissue weight). In contrast, free HF in the blood circulation could be incorporated efficiently and highly accumulated in normal lung tissue (598.4 ng/g of tissue weight). These results clearly demonstrate the preferential accumulation of HFm in tumors.

The administration of HFm reproducibly resulted in lower accumulation of HF in the spleen and liver than the administration of free HF (Fig 19B). This significantly lower accumulation of HF in normal tissues following HFm administration must be the reason underlying the lower systemic toxicity of HFm. I also found that HFm administration gave rise to markedly higher levels of HF accumulation in spleen and liver than in the lungs. The reason for these differences is currently unclear. One plausible explanation is that the EPR effect displayed in case of polymeric micelles is strictly operating in the lung tissue, which seems to be an advantage of the use of HFm against lung cancers.

3.7. Low-dose HF/HFm therapy suppresses Nrf2-activated tumors but not as effectively as high-dose treatment

The results thus far demonstrate that HFm treatment has better efficacy in lung cancer with much lower adverse effects than free HF treatment at the MTD. To ascertain whether these results are reproducible with doses of HF lower than the MTD in lung cancer and to verify whether HFm

produces efficacy similar to that of HF even at the basal effective dose (BED), I next examined HF and HFm treatments in lung cancer-bearing mice administered at the BED, *i.e.,* 0.25 mg/kg bw.

I employed the same protocol as used in the previous subsection in which KRAS-driven lung adenocarcinoma was allowed to grow for 17 weeks after which mice were treated with saline, HF (0.25 mg/kg) or HFm (0.25 mg/kg) every other day for four times in total (Fig 20A). As was the case with high-dose (0.75 mg/kg) treatment, HF and HFm at the BED also effectively reduced lung weight (Fig 20B). I stained lung sections with HE (Fig 21A) and found that the tumor area was significantly reduced by both HF treatment and HFm treatment (Fig 21B), even at the BED, although tumor suppression appeared to be much weaker at a lower dose or the BED than that at a higher dose or the MTD. At the higher dose, tumor areas were decreased by 9.95% (saline versus HF) and 15.77% (saline versus HFm), whereas at the low dose, tumor areas were decreased by only 7.42% (saline versus HF) and 9.49% (saline versus HFm). Similarly, at the higher dose, lung weight was decreased by 37.6% and 49.6% in HF- and HFm-treated mice, respectively, while the decreases were 25.7% (saline versus HF) and 22.8% (saline versus HFm) with the low-dose regimen (Figs 13B and 20B).

Even with 0.25 mg/kg bw treatment, the number of papillary lesions was much lower with HF or HFm treatment than with saline treatment (Fig 21A; lower panel and Fig 21C). The number of solid tumors was significantly lower after 0.25 mg/kg bw HF or HFm administration than after vehicle treatment (Fig 21C). However, in contrast to the changes observed with the high-dose therapy (Fig 14C), solid tumors were not completely absent with the low-dose therapy, and efficacy was comparable between the HF and HFm treatments. While the body weight changes in all mouse cohorts remained comparable upon treatment (Fig 22A), low-dose treatment with HF

significantly reduced the white blood cell marker. HF treatment at 0.25 mg/kg bw did not affect the red blood cell level. Of note, this adverse effect was rescued by the use of HFm (Fig 22B). These results indicate that HF treatment at the BED still causes severe toxicity to the white blood cell count. An important observation here is that HFm treatment at this lower dose shows therapeutic efficacy comparable to that achieved with the same dose of HF. Thus, these results demonstrate that HFm acts as a safer and stronger therapeutic agent than HF and that HFm can be available for use in higher dose regimens.

4. Discussion

Aberrant NRF2 activation is frequently observed in various types of cancers, leading to coordinated expression of various cytoprotective genes. Such NRF2 hyperactivation confers resistance to chemo/radiotherapy to cancer cells and results in malignancy (11,14). Because of the lack of approved therapies to treat these NRF2-activated cancers, there is an important unmet clinical need to find a viable therapy to treat patients with such tumors. My laboratory previously identified HF as a potent NRF2 inhibitor (16) and provided preclinical proof-of-concept evidence of its role as an anticancer chemosensitizer. In this study, however, I also found that high-dose HF administration to WT mice caused severe dose-dependent toxicity, including significant decreases in hematopoietic and immune cells in the spleen, thymus, and bone marrow. Therefore, to overcome these adverse effects, my collaborators designed HFm, in which HF is encapsulated into micelles to reduce the systemic toxicity of HF while maintaining its tumor-suppressive properties. I examined the efficacy and adverse effects of HFm employing $Keap1^{FB/FB}$::$Kras^{G12D}$ tumor-bearing model mice and found that HFm decreased the tumor burden without causing immune suppression or reductions in hematopoietic cells. I also confirmed through LC-MS/MS experiments that this reduction in adverse effects was caused by the ability of HFm to release HF from the core in a slow and sustained manner. These results support the notion that the application of an elaborate nanomedicine makes HFm a suitable drug for treating NRF2-activated cancers.

In this study, I found that the administration of HF caused significant decreases in immune and hematopoietic cell populations. While there are several papers that describe HF toxicity at high doses, to the best of our knowledge, there is no description of the immunosuppression and hemopoietic cell suppression mediated by HF. I surmised that there might be two pathways leading to this toxicity: the Nrf2-dependent pathway and the Nrf2-independent pathway. I speculated that

the Nrf2-independent pathway may be linked to immunosuppression facilitated by the GCN2-eIF2 axis. The asparaginase-induced amino acid starvation response has been reported to cause decrease in thymus and spleen sizes and depletion of B cells, CD4+ T cells and CD8+ T cells by inducing enhanced eIF2 phosphorylation in a GCN2-dependent manner (36). Since the HF-mediated suppression of Nrf2 is driven by eIF2 phosphorylation via GCN2 (16,37), it seems plausible that the decreases in immune and hematopoietic cell populations might be caused through the same pathway.

Nrf2 deficiency causes a decrease in hematopoietic stem cells (38,39). I also found a moderate decrease in progenitor cells (c-Kit+) in the bone marrow. Therefore, I speculated that the reduction occurs in an Nrf2-dependent manner. Notably, while most of the cell populations investigated in this study are immune cells, modest decreases in red blood cells, hematocrit levels and erythroblasts were also observed, indicating that HF-induced cell death may occur widely, implying pan cellular HF toxicity. The HF-induced toxicity to lymphoid cells, including CD4 single-positive cells, CD8 single-positive cells, and B cells, was more pronounced than that to myeloid-derived macrophages and neutrophils. However, the mechanisms underlying this observation remain to be clarified. Of note, in accordance with our earlier hypothesis, Nrf2 inhibition using an elaborate tumor-oriented nanomedicine appears to be an excellent approach to treat Nrf2-activated cancers and achieve a maximal effect of chemotherapy.

The pharmacodynamics and pharmacokinetics studies conducted using LC-MS/MS analysis in Spleen, Liver and lung in this study clearly showed that free HF accumulates in these organs rather quickly in large amounts leading to toxicity. Whereas in case of HFm because of slow and sustained release of HF such side effects are absent. Checking HF levels in plasma and urine would have helped in better understanding of HFm metabolism. I assume in case of HFm,

higher HF plasma concentration (compared to free HF) would have been observed given its ability to circulate in the bloodstream for a longer time. On the other hand, urine would have lower HF levels in case of HFm (compared to free HF) because of lower non tumor tissue accumulation. Further experiments are warranted to check this claim.

The initial experiments (Fig. 7 to Fig. 10) done in this study to determine the maximal tolerable dose (MTD) of HF were performed on the WT mice. These mice interestingly showed lower levels of different white blood cell and hematopoietic cell markers compared to the tumor bearing mice models. I speculate this increase in case of $Keap1^{FB/FB}$::$Kras^{G12D}$ mice cell number might be because of presence of tumor. Nevertheless, a question might arise if HFm administration would cause toxicity in WT mice or would it be absent like in the case of tumor bearing models ($Keap1^{FB/FB}$::$Kras^{G12D}$). I had performed some preliminary study wherein I had treated WT mice with 0.8mg/kg of HFm (not 0.75 mg/kg used in the whole study). In these set of experiments WT mice treated with 0.8 mg/kg HFm did not show any apparent difference in white blood cell, red blood cell or hemoglobin values. On the other hand, consistent with previous data in this thesis, WT mice treated with 0.8mg/kg HF did have significant lower levels of all these parameters (Fig 23). These data clearly shows that HFm is well tolerated without any adverse toxicity in WT mice and this phenomenon is not only limited to tumor bearing models.

High-dose HF and HFm completely eradicated grade III solid tumors in $Keap1^{FB/FB}$::$Kras^{G12D}$ tumor-bearing model mice. Assuming that a multitude of tumors arise in the lungs of these model mice, I speculated that Nrf2 inhibition mostly eradicated Nrf2-activated cancers and that most of the remaining tumors harbored only $Kras^{G12D}$ mutations. Kras-mutant

tumors without Nrf2 activation are known to be less invasive (40), so the lung sections of mice treated with HF or HFm had no solid tumors. An alternative explanation is the involvement of the metalloproteinase-2 (MMP-2) pathway, as HF has been shown to suppress the expression of MMP-2 (40). Since MMP-2 is responsible for the membrane invasion and metastasis of tumors, I speculated that HF may act to decrease MMP-2 levels, resulting in the elimination of solid tumors. Notably, HF is widely used as an antibiotic for animals in veterinary medicine (41,42) and has also been shown to possess anticancer and antimetastatic properties in various *in vivo* studies. HF has been reported to inhibit the TGF-β signaling pathway, to limit the progression of melanoma bone metastases (43) and to suppress the metastasis of bladder carcinoma by suppressing MMP-2 expression (40). HF has also gone through various phase II human trials as a therapy for AIDS-related Kaposi's sarcoma and fibrotic diseases (44-48). Based on the present study, I propose that HFm may have better efficacy and fewer adverse effects than other therapies, in addition to targeting currently untreatable NRF2-activated tumors.

Here it is important to note that since HF has been shown to suppress tumor activity by Nrf2-independent pathways (36,39), it is quite possible that in my model decrease in tumor burden was caused by both Nrf2-dependent and Nrf2-independent mechanisms. In fact, my preliminary Nqo1 Immunohistochemistry staining data shows that both Nqo1-positive (cancer cells with both Keap1 and Kras mutations) and Nqo1 negative (cancer cells with only Kras mutations) tumors showed decreasing trend on HF/HFm treatment (Fig 24). It has been previously reported in the literature (49) that co-treatment of Kras tumors with a AKT inhibitor-MK2206 (which blocks downstream Nrf2 expression) and ASN depletion through L-asparaginase together downregulates ATF4 production (which is dependent on GCN2-eIF2α axis for its translation) leading to suppression of Kras tumor growth by asparagine starvation. Since HF impedes Nrf2 transcription

and is also responsible for downregulation of GCN2- eIF2α axis, I speculate that suppression of Nqo1-negative tumors in my experiments in the HF/HFm treated $Keap1^{FB/FB}$::$Kras^{G12D}$ model mice was mediated by ATF4 transcription inhibition.

However, since Nrf2 mutated tumors have been shown to be resistant to known chemotherapeutic agents (14), tumor suppression wouldn't have been possible without decrease in Nrf2 protein levels in Nqo1-positive tumors. Additionally, when mRNA levels of downstream Nrf2 gene (Nqo1) in tumor bearing mice lung was measured upon Saline/HF (0.25mg/kg) or HFm (0.25mg/kg) treatment , a decreasing trend was observed in the case of HF and HFm groups (Fig 25). This clearly indicates Nrf2 downregulation plays a major role in tumor reduction in these mice. Hence, I feel while the decrease in Nqo1-positive tumors by HF/HFm treatment in my model was Nrf2 dependent, Nqo1-negative tumors decreased due to a Nrf2 independent pathway (possibly through ATF4 transcription inhibition). Further examinations are required to prove this claim.

Additionally, a question might arise if $Kras^{G12D}$ tumor bearing model mice would also exhibit lower tumor burden on HF/HFm treatment as well. Since my preliminary experiments show decrease in Nqo1- negative tumors, I would speculate HF/HFm would indeed decrease $Kras^{G12D}$ tumors by decreasing ATF4 levels.

In summary, I showed in this study that HFm efficaciously eradicated NRF2-activated tumors in the lungs without any apparent systemic toxicity. These promising results support the translation of HFm into human studies, given the high clinical need for NRF2 inhibitors.

References

1. Itoh K, Chiba T, Takahashi S, Ishii T, Igarashi K, Katoh Y*, et al.* An Nrf2/small Maf heterodimer mediates the induction of phase II detoxifying enzyme genes through antioxidant response elements. Biochem Biophys Res Commun **1997**;236:313-22
2. Kobayashi A, Kang MI, Okawa H, Ohtsuji M, Zenke Y, Chiba T*, et al.* Oxidative stress sensor Keap1 functions as an adaptor for Cul3-based E3 ligase to regulate proteasomal degradation of Nrf2. Mol Cell Biol **2004**;24:7130-9
3. Mitsuishi Y, Taguchi K, Kawatani Y, Shibata T, Nukiwa T, Aburatani H*, et al.* Nrf2 redirects glucose and glutamine into anabolic pathways in metabolic reprogramming. Cancer Cell **2012**;22:66-79
4. Otsuki A, Suzuki M, Katsuoka F, Tsuchida K, Suda H, Morita M*, et al.* Unique cistrome defined as CsMBE is strictly required for Nrf2-sMaf heterodimer function in cytoprotection. Free Radic Biol Med **2016**;91:45-57
5. Rushmore TH, Morton MR, Pickett CB. The antioxidant responsive element. Activation by oxidative stress and identification of the DNA consensus sequence required for functional activity. J Biol Chem **1991**;266:11632-9
6. Friling RS, Bensimon A, Tichauer Y, Daniel V. Xenobiotic-inducible expression of murine glutathione S-transferase Ya subunit gene is controlled by an electrophile-responsive element. Proc Natl Acad Sci U S A **1990**;87:6258-62
7. Chorley BN, Campbell MR, Wang X, Karaca M, Sambandan D, Bangura F*, et al.* Identification of novel NRF2-regulated genes by ChIP-Seq: influence on retinoid X receptor alpha. Nucleic Acids Res **2012**;40:7416-29
8. Hirotsu Y, Katsuoka F, Funayama R, Nagashima T, Nishida Y, Nakayama K*, et al.* Nrf2-MafG heterodimers contribute globally to antioxidant and metabolic networks. Nucleic Acids Res **2012**;40:10228-39
9. Kandoth C, McLellan MD, Vandin F, Ye K, Niu B, Lu C*, et al.* Mutational landscape and significance across 12 major cancer types. Nature **2013**;502:333-9
10. Sanchez-Vega F, Mina M, Armenia J, Chatila WK, Luna A, La KC*, et al.* Oncogenic Signaling Pathways in The Cancer Genome Atlas. Cell **2018**;173:321-37.e10
11. Shibata T, Ohta T, Tong KI, Kokubu A, Odogawa R, Tsuta K*, et al.* Cancer related mutations in NRF2 impair its recognition by Keap1-Cul3 E3 ligase and promote malignancy. Proc Natl Acad Sci U S A **2008**;105:13568-73
12. Network CGAR. Comprehensive genomic characterization of squamous cell lung cancers. Nature **2012**;489:519-25
13. Network CGAR, University AWGA, Agency BC, Hospital BaWs, Institute B, University B*, et al.* Integrated genomic characterization of oesophageal carcinoma. Nature **2017**;541:169-75
14. Goldstein LD, Lee J, Gnad F, Klijn C, Schaub A, Reeder J*, et al.* Recurrent Loss of NFE2L2 Exon 2 Is a Mechanism for Nrf2 Pathway Activation in Human Cancers. Cell Rep **2016**;16:2605-17

15. Bamford S, Dawson E, Forbes S, Clements J, Pettett R, Dogan A*, et al.* The COSMIC (Catalogue of Somatic Mutations in Cancer) database and website. Br J Cancer **2004**;91:355-8
16. Tsuchida K, Tsujita T, Hayashi M, Ojima A, Keleku-Lukwete N, Katsuoka F*, et al.* Halofuginone enhances the chemo-sensitivity of cancer cells by suppressing NRF2 accumulation. Free Radic Biol Med **2017**;103:236-47
17. Hiramoto K, Satoh H, Suzuki T, Moriguchi T, Pi J, Shimosegawa T*, et al.* Myeloid lineage-specific deletion of antioxidant system enhances tumor metastasis. Cancer Prev Res (Phila) **2014**;7:835-44
18. Satoh H, Moriguchi T, Taguchi K, Takai J, Maher JM, Suzuki T*, et al.* Nrf2-deficiency creates a responsive microenvironment for metastasis to the lung. Carcinogenesis **2010**;31:1833-43
19. Satoh H, Moriguchi T, Saigusa D, Baird L, Yu L, Rokutan H*, et al.* NRF2 Intensifies Host Defense Systems to Prevent Lung Carcinogenesis, but After Tumor Initiation Accelerates Malignant Cell Growth. Cancer Res **2016**;76:3088-96
20. Hayashi M, Kuga A, Suzuki M, Panda H, Kitamura H, Motohashi H*, et al.* Microenvironmental Activation of Nrf2 Restricts the Progression of Nrf2-Activated Malignant Tumors. Cancer Res **2020**;80:3331-44
21. Yokoyama M, Okano T, Sakurai Y, Fukushima S, Okamoto K, Kataoka K. Selective delivery of adriamycin to a solid tumor using a polymeric micelle carrier system. J Drug Target **1999**;7:171-86
22. Lavasanifar A, Samuel J, Kwon GS. Poly(ethylene oxide)-block-poly(L-amino acid) micelles for drug delivery. Adv Drug Deliv Rev **2002**;54:169-90
23. Nishiyama N, Kato Y, Sugiyama Y, Kataoka K. Cisplatin-loaded polymer-metal complex micelle with time-modulated decaying property as a novel drug delivery system. Pharm Res **2001**;18:1035-41
24. Maeda H. The enhanced permeability and retention (EPR) effect in tumor vasculature: the key role of tumor-selective macromolecular drug targeting. Adv Enzyme Regul **2001**;41:189-207
25. Nakanishi T, Fukushima S, Okamoto K, Suzuki M, Matsumura Y, Yokoyama M*, et al.* Development of the polymer micelle carrier system for doxorubicin. J Control Release **2001**;74:295-302
26. Maeda H, Sawa T, Konno T. Mechanism of tumor-targeted delivery of macromolecular drugs, including the EPR effect in solid tumor and clinical overview of the prototype polymeric drug SMANCS. J Control Release **2001**;74:47-61
27. Kim BS, Naito M, Chaya H, Hori M, Hayashi K, Min HS*, et al.* Noncovalent Stabilization of Vesicular Polyion Complexes with Chemically Modified/Single-Stranded Oligonucleotides and PEG-. Biomacromolecules **2020**;21:4365-76
28. Baird L, Suzuki T, Takahashi Y, Hishinuma E, Saigusa D, Yamamoto M. Geldanamycin-Derived HSP90 Inhibitors Are Synthetic Lethal with NRF2. Mol Cell Biol **2020**;40
29. Jackson EL, Willis N, Mercer K, Bronson RT, Crowley D, Montoya R*, et al.* Analysis of lung tumor initiation and progression using conditional expression of oncogenic K-ras. Genes Dev **2001**;15:3243-8

30. Blake DJ, Singh A, Kombairaju P, Malhotra D, Mariani TJ, Tuder RM*, et al.* Deletion of Keap1 in the lung attenuates acute cigarette smoke-induced oxidative stress and inflammation. Am J Respir Cell Mol Biol **2010**;42:524-36
31. DuPage M, Dooley AL, Jacks T. Conditional mouse lung cancer models using adenoviral or lentiviral delivery of Cre recombinase. Nat Protoc **2009**;4:1064-72
32. Matus JL, Boison JO. A multi-residue method for 17 anticoccidial drugs and ractopamine in animal tissues by liquid chromatography-tandem mass spectrometry and time-of-flight mass spectrometry. Drug Test Anal **2016**;8:465-76
33. Wang J, Mao W, Lock LL, Tang J, Sui M, Sun W*, et al.* The Role of Micelle Size in Tumor Accumulation, Penetration, and Treatment. ACS Nano **2015**;9:7195-206
34. Stecklair KP, Hamburger DR, Egorin MJ, Parise RA, Covey JM, Eiseman JL. Pharmacokinetics and tissue distribution of halofuginone (NSC 713205) in CD2F1 mice and Fischer 344 rats. Cancer Chemother Pharmacol **2001**;48:375-82
35. Inamura K. Lung Cancer: Understanding Its Molecular Pathology and the 2015 WHO Classification. Front Oncol **2017**;7:193
36. Bunpo P, Cundiff JK, Reinert RB, Wek RC, Aldrich CJ, Anthony TG. The eIF2 kinase GCN2 is essential for the murine immune system to adapt to amino acid deprivation by asparaginase. J Nutr **2010**;140:2020-7
37. Sundrud MS, Koralov SB, Feuerer M, Calado DP, Kozhaya AE, Rhule-Smith A*, et al.* Halofuginone inhibits TH17 cell differentiation by activating the amino acid starvation response. Science **2009**;324:1334-8
38. Merchant AA, Singh A, Matsui W, Biswal S. The redox-sensitive transcription factor Nrf2 regulates murine hematopoietic stem cell survival independently of ROS levels. Blood **2011**;118:6572-9
39. Murakami S, Suzuki T, Harigae H, Romeo PH, Yamamoto M, Motohashi H. NRF2 Activation Impairs Quiescence and Bone Marrow Reconstitution Capacity of Hematopoietic Stem Cells. Mol Cell Biol **2017**;37
40. Elkin M, Reich R, Nagler A, Aingorn E, Pines M, de-Groot N*, et al.* Inhibition of matrix metalloproteinase-2 expression and bladder carcinoma metastasis by halofuginone. Clin Cancer Res **1999**;5:1982-8
41. Naciri M, Mancassola R, Yvoré P, Peeters JE. The effect of halofuginone lactate on experimental Cryptosporidium parvum infections in calves. Vet Parasitol **1993**;45:199-207
42. Villacorta I, Peeters JE, Vanopdenbosch E, Ares-Mazás E, Theys H. Efficacy of halofuginone lactate against Cryptosporidium parvum in calves. Antimicrob Agents Chemother **1991**;35:283-7
43. Juárez P, Mohammad KS, Yin JJ, Fournier PG, McKenna RC, Davis HW*, et al.* Halofuginone inhibits the establishment and progression of melanoma bone metastases. Cancer Res **2012**;72:6247-56
44. Koon HB, Fingleton B, Lee JY, Geyer JT, Cesarman E, Parise RA*, et al.* Phase II AIDS Malignancy Consortium trial of topical halofuginone in AIDS-related Kaposi sarcoma. J Acquir Immune Defic Syndr **2011**;56:64-8

45. Elkin M, Ariel I, Miao HQ, Nagler A, Pines M, de-Groot N*, et al.* Inhibition of bladder carcinoma angiogenesis, stromal support, and tumor growth by halofuginone. Cancer Res **1999**;59:4111-8
46. Pines M, Nagler A. Halofuginone: a novel antifibrotic therapy. Gen Pharmacol **1998**;30:445-50
47. McGaha T, Kodera T, Phelps R, Spiera H, Pines M, Bona C. Effect of halofuginone on the development of tight skin (TSK) syndrome. Autoimmunity **2002**;35:277-82
48. Pines M, Snyder D, Yarkoni S, Nagler A. Halofuginone to treat fibrosis in chronic graft-versus-host disease and scleroderma. Biol Blood Marrow Transplant **2003**;9:417-25
49. Gwinn DM, Lee AG, Briones-Martin-Del-Campo M, Conn CS, Simpson DR, Scott AI*, et al.* Oncogenic KRAS Regulates Amino Acid Homeostasis and Asparagine Biosynthesis via ATF4 and Alters Sensitivity to L-Asparaginase. Cancer Cell **2018**;33:91-107.e6

Figures

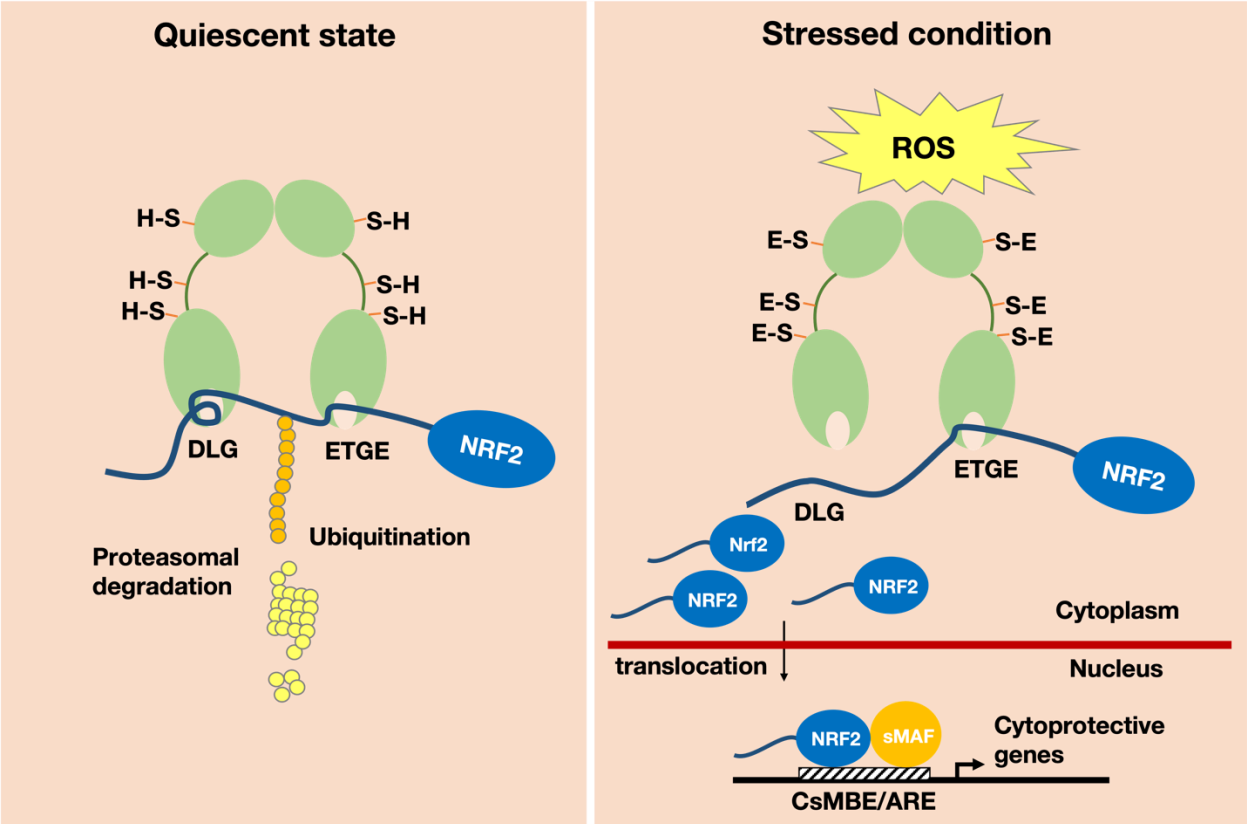

Fig. 1. Structural and functional basis of the KEAP1-NRF2 system. The transcription factor NRF2 is a master regulator of the response to oxidative and electrophilic stresses in the human body. Under quiescent conditions, NRF2 is targeted for ubiquitination by the principal negative regulator KEAP1 (left). KEAP1 is a cysteine-thiol-enriched molecule that is the stress sensor and ubiquitin ligase of NRF2. Reactive oxygen species (ROS) and electrophiles induce modification of the cysteine-thiol moieties on KEAP1, facilitating the escape of NRF2 from ubiquitination. NRF2 thus accumulates in the cytoplasm, leading to its translocation into the nucleus. NRF2 forms a heterodimer with the sMAF molecule and binds to a CNC–sMaf binding elements (CsMBE) or antioxidant-responsive element (ARE) motif, resulting in the transcription of a battery of antioxidant, cytoprotective, metabolizing and anti-inflammatory enzymes (right).

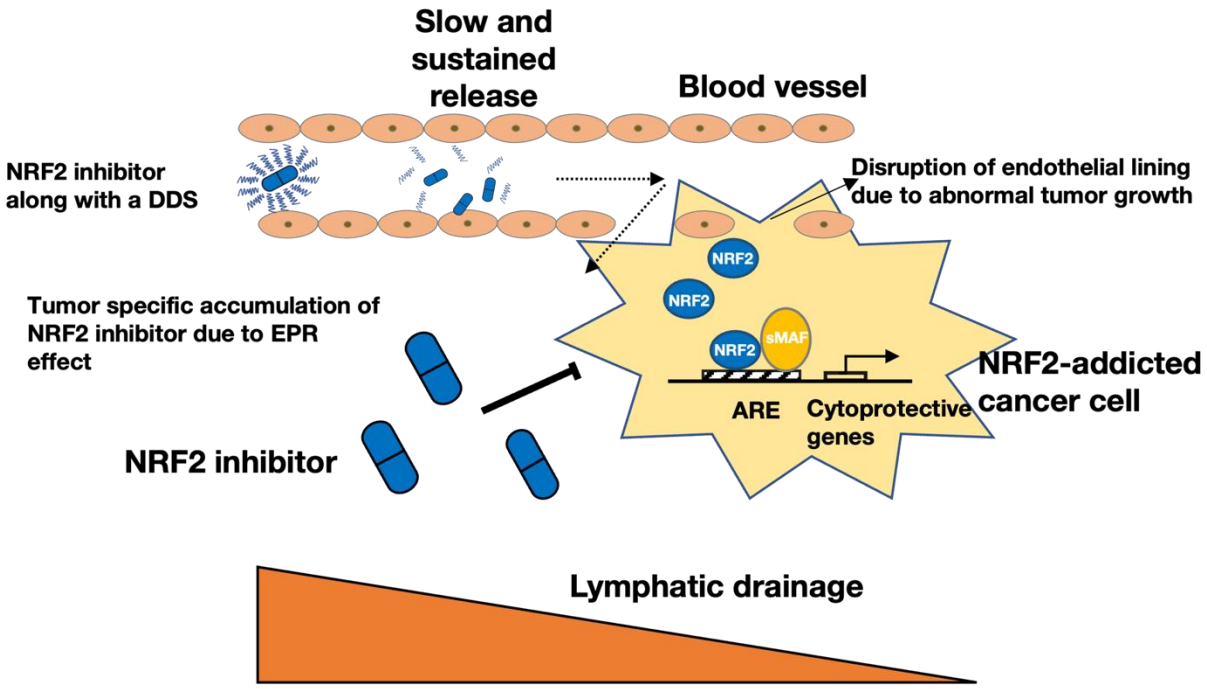

Fig. 2. Therapeutic strategies to control NRF2-addicted cancers. In the tumor, NRF2 inhibitors help suppress tumor growth and metastasis by decreasing NRF2 protein levels. However, problems posed by systemic NRF2 inhibition can be prevented by using NRF2 inhibitors in an elaborate drug delivery system designed to achieve high cancer tissue specificity through the enhanced permeability and retention (EPR) effect.

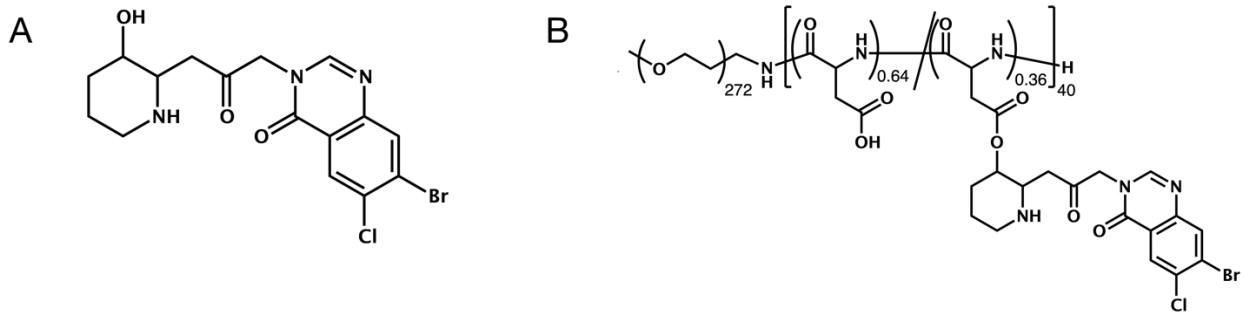

Halofuginone (HF) **Halofuginone micelle** (HFm)

Fig. 3. Chemical structure of (A) Halofuginone (HF) and (B) Halofuginone micelle (HFm).

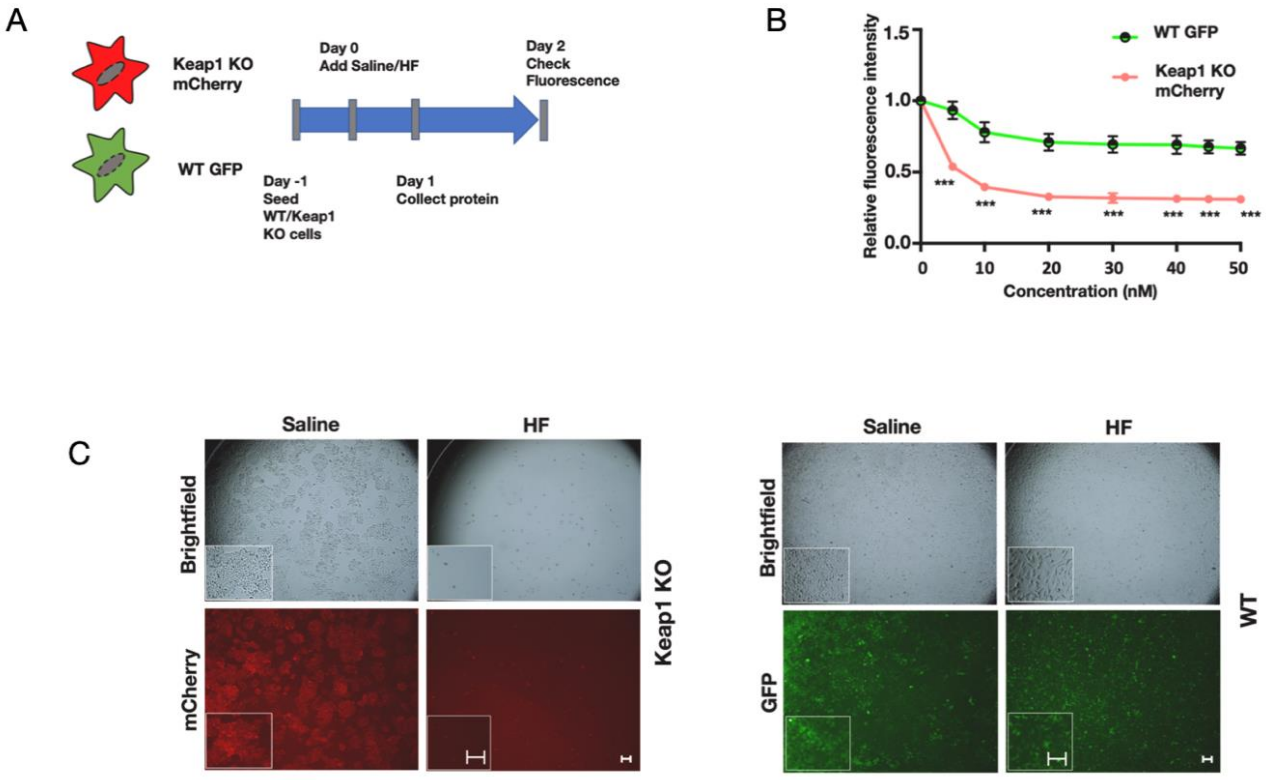

Fig. 4. HF targets Nrf2 activated cancer cells *in vitro* (A) Schematic representation of the HF/saline treatment protocol of Keap1 KO mCherry and WT GFP Hepa1 cells. (B) The cell viability of the Keap1 KO mCherry and WT GFP cells was determined using fluorescence intensity 48 hours after the introduction of HF at different concentrations. The fluorescence levels were normalized to saline treated control fluorescence levels (n=3). Student t-test, *P≤0.05, **P≤0.01, ***P≤0.001. (C) Representative images of cells 48 hours after saline or HF (50 nM) treatment. Scale- 200μm.

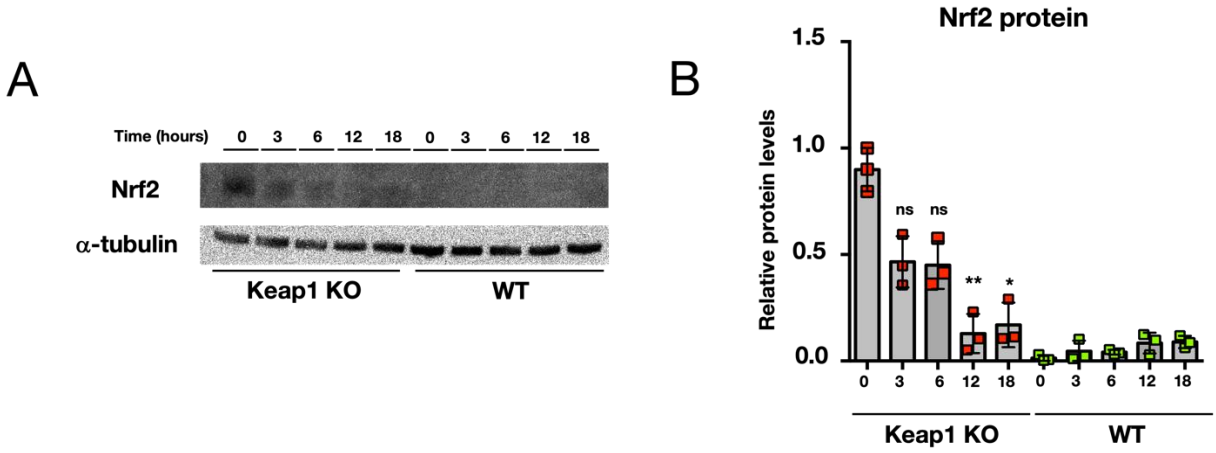

Fig. 5. HF suppresses Nrf2 accumulation in Nrf2 activated Hepa1 cells. (A) Nrf2 protein levels in Keap1 KO mCherry and WT GFP cells after HF treatment (50 nM), for the indicated time periods. (B) Quantification of Nrf2 protein levels in whole-cell lysates of Keap1 KO mCherry and WT GFP cells exposed to 50 nM HF for the indicated periods (n=3). Each time point is compared to control (0 hour) of the same group (Keap1 KO or WT). Non-parametric Kruskal-Wallis test, **P≤0.05, **P≤0.01, ***P≤0.001. Nrf2 protein were normalized to the α-tubulin levels. Graphed data are presented as means±SD.

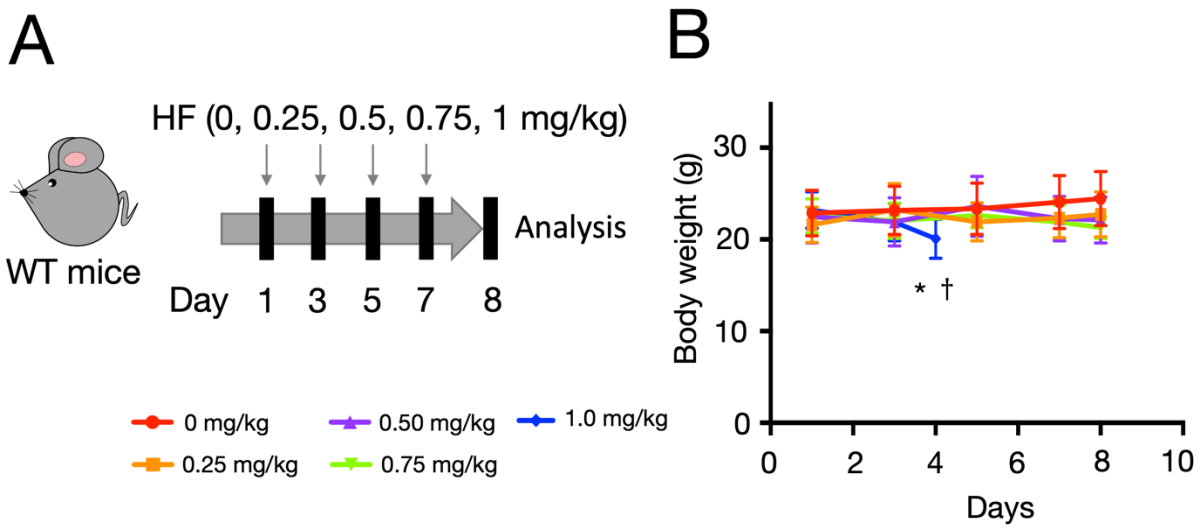

Fig. 6. Dose dependent *in-vivo* toxicity assessment of HF. (A) Experimental strategy to determine the maximum tolerable dose (MTD) of HF. (B) Body weight changes after intravenous HF injections (n=7). Mice treated with 1 mg/kg HF (blue line) were moribund and were euthanized before the end of the experiment; Student t-test, *P≤0.05, **P≤0.01, ***P≤0.001, Day 1 vs. Day 4, † 1 of the 8 mice died at 1mg/kg.

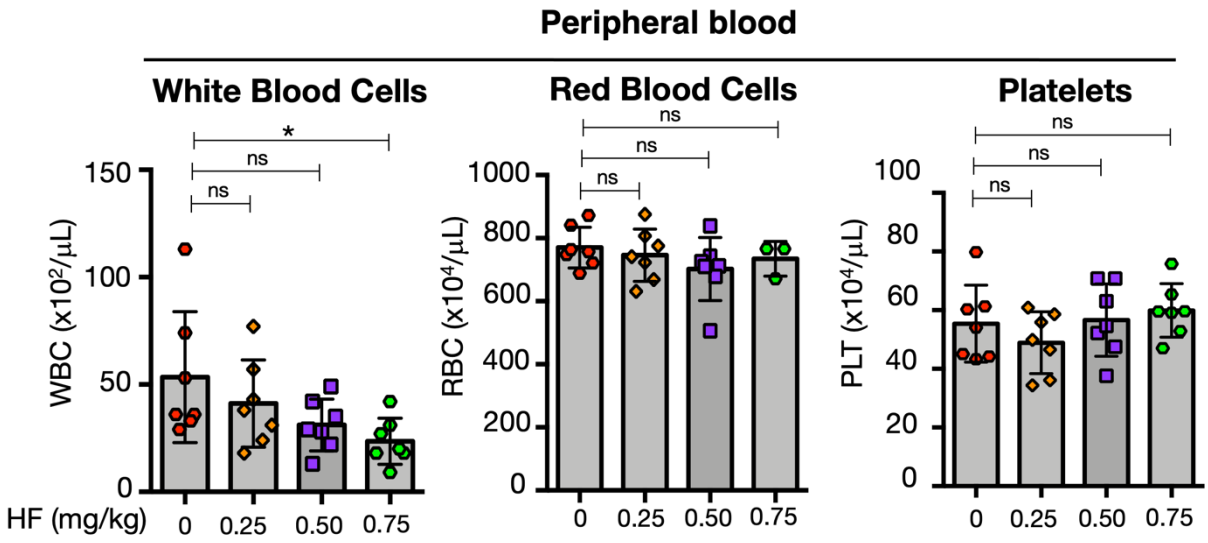

Fig. 7. HF administration causes dose-dependent decrease in the white blood cell count. White blood cell, red blood cell and platelet counts in the peripheral blood of the mice treated with varied dose of HF; Non-parametric Kruskal-Wallis test, *P≤0.05, **P≤0.01, ***P≤0.001, ns=not significant.

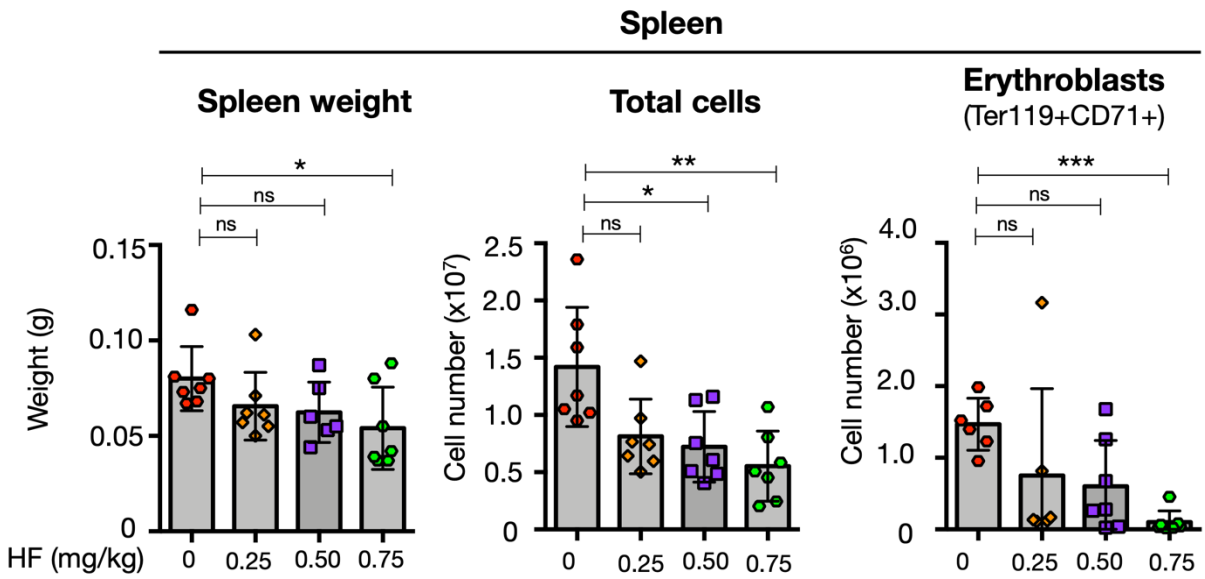

Fig. 8. HF injection produced substantial dose-dependent declines in total splenocytes and erythroblasts (Ter119+CD71+) in the spleen. Spleen weight, total splenic cell count and erythroblasts (Ter119+CD71+) after HF treatment at incremental dosage. Cells were isolated from the spleen of the mice; Non-parametric Kruskal-Wallis test, *P≤0.05,**P≤0.01,***P≤0.001 ns=not significant.

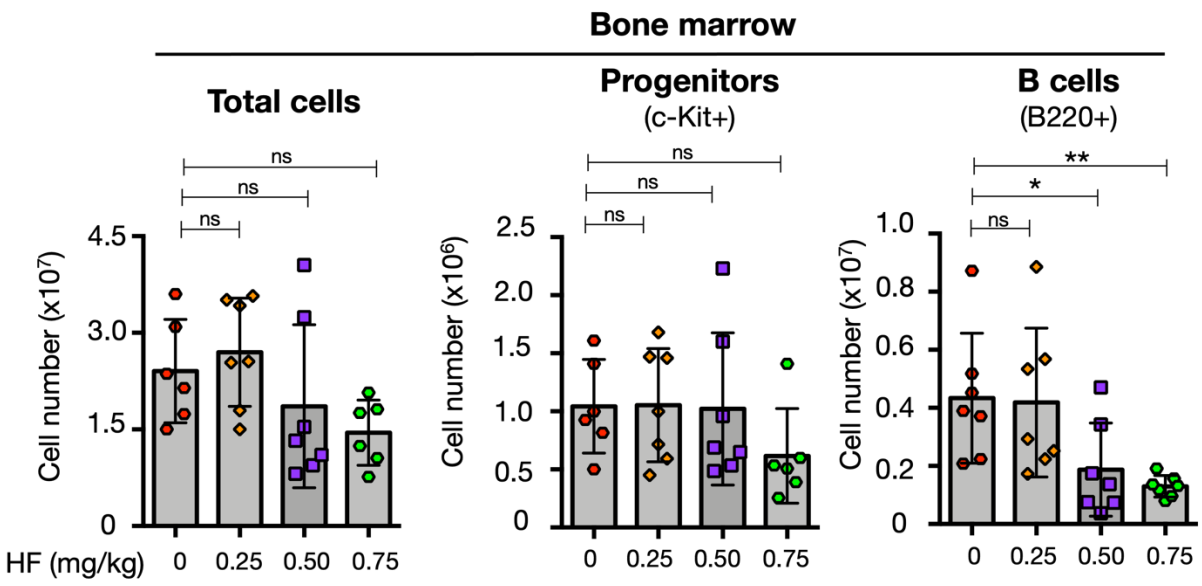

Fig. 9. HF administration causes Bone marrow suppression in dose-dependent manner. Total, Progenitors (c-Kit+) and B (B220+) cells from bone marrow of mice treated with different concentrations of HF; Non-parametric Kruskal-Wallis test, *P≤0.05, **P≤0.01, ***P≤0.001, ns=not significant.

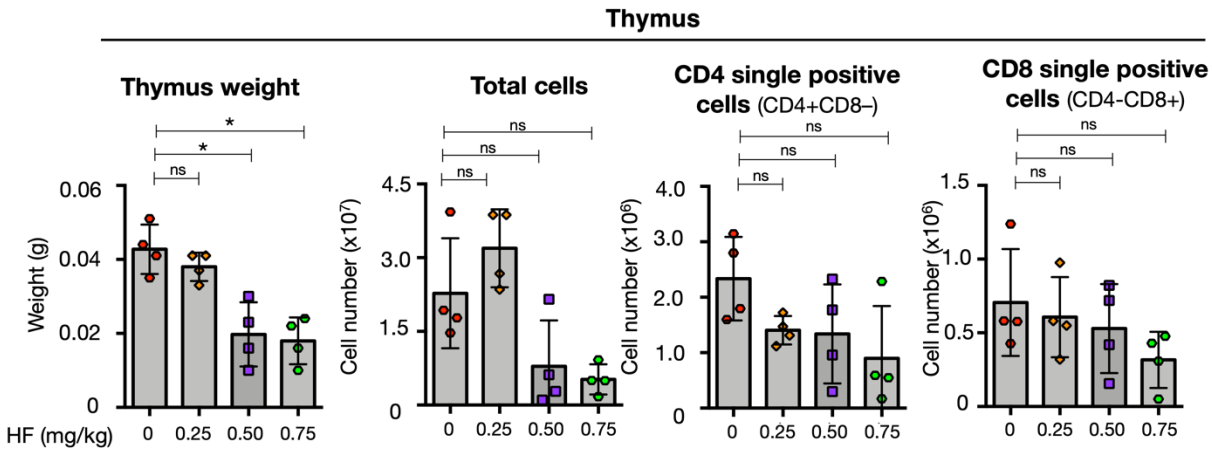

Fig. 10. HF inoculation causes toxicity in thymus. Thymus weight, total thymic cell count, CD4 single positive (CD4+CD8–) and CD8 single positive (CD4–CD8+) cell number after the HF treatment. Cells were isolated from the thymus; Non-parametric Kruskal-Wallis test, *P≤0.05, **P≤0.01, ***P≤0.001, ns=not significant. Graphed data are presented as means±SD.

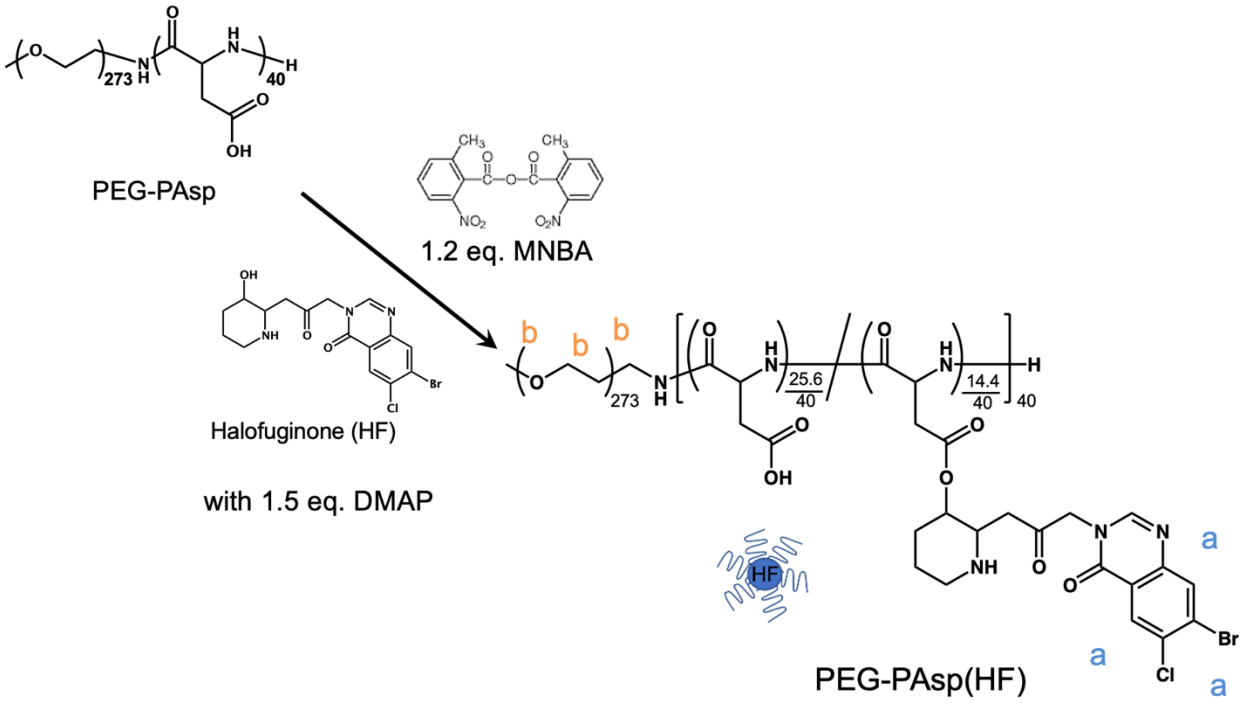

Fig. 11. Chemical synthesis of Halofuginone micelle (HFm). PEG-PAsp(HF) [HFm] is obtained by a reaction involving 2-Methyl-6-nitrobenzoic anhydride (MNBA; 1.2 equivalents to Asp) and 2,2-dimethoxypropane (DMAP;1.5 equivalents to Asp) along with the PEG-PAsp solution (PEG-PAsp dissolved in *N*,*N*-dimethylformamide). 40 mentioned in the HFm chemical structure represents the degree of polymerization of polyaspartic acid (PAsp). 14.4 are the number of HF molecules introduced in each polymer. 273 is the atomic weight of the polymer. "a" and "b" corresponds to benzylic protons of HF and the polymer protons respectively (the peaks of which are observed in the ^{1}H NMR spectrum described in the next figure). The blue cartoon alongside the HFm chemical structure represents the aggregate this polymer forms; HF is situated at the center of this complex surrounded by the polymer forming a micelle.

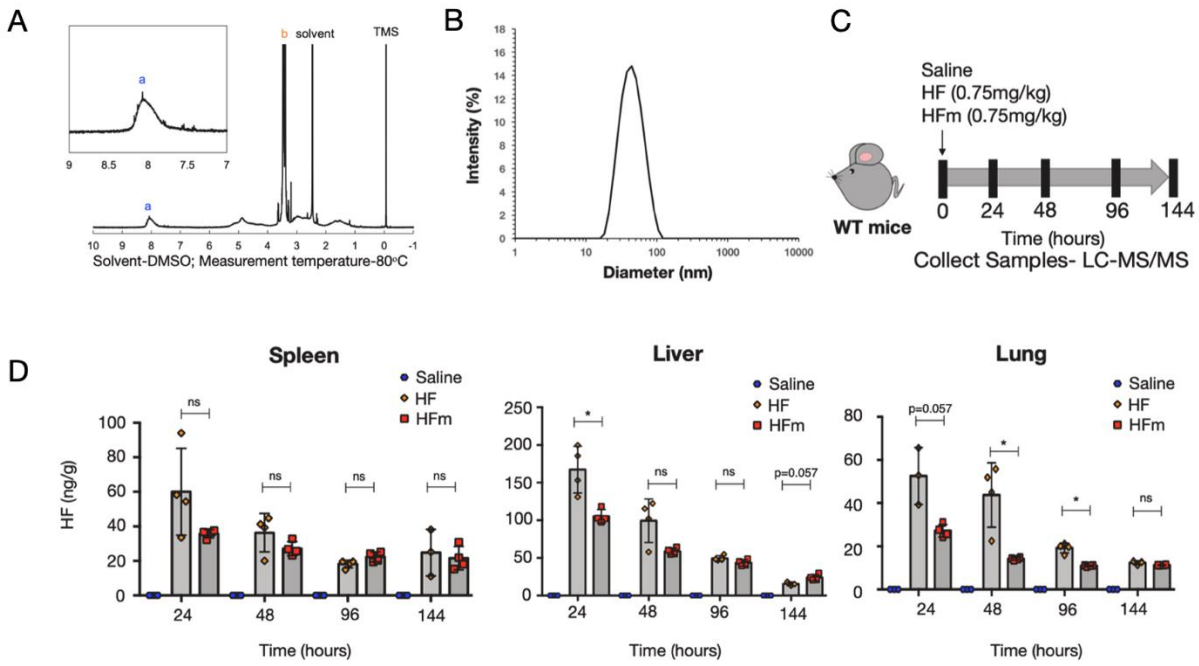

Fig. 12. Pharmacokinetics and biodistribution of HF-loaded polymeric micelle (HFm). (A) ^{1}H NMR spectrum of PEG-PAsp(HF). a represents the HF signal. "a" and "b" corresponds to benzylic protons of HF and the polymer protons, respectively. (B) Size distribution histogram of HFm determined by dynamic light scattering. (C) Experimental design for the LC-MS/MS analysis of WT mice (8-12 weeks old) treated with one shot of saline, HF or HFm (both 0.75 mg/kg). Spleen, liver, and lung was collected at 0, 24, 48, 96 and 144 hours after intravenous injection. (D) HF accumulation in spleen, liver, and lung tissues after HF and HFm (0.75 mg/kg) treatment at different time points. *P≤0.05, ns=not significant (Non-parametric Mann-Whitney test).

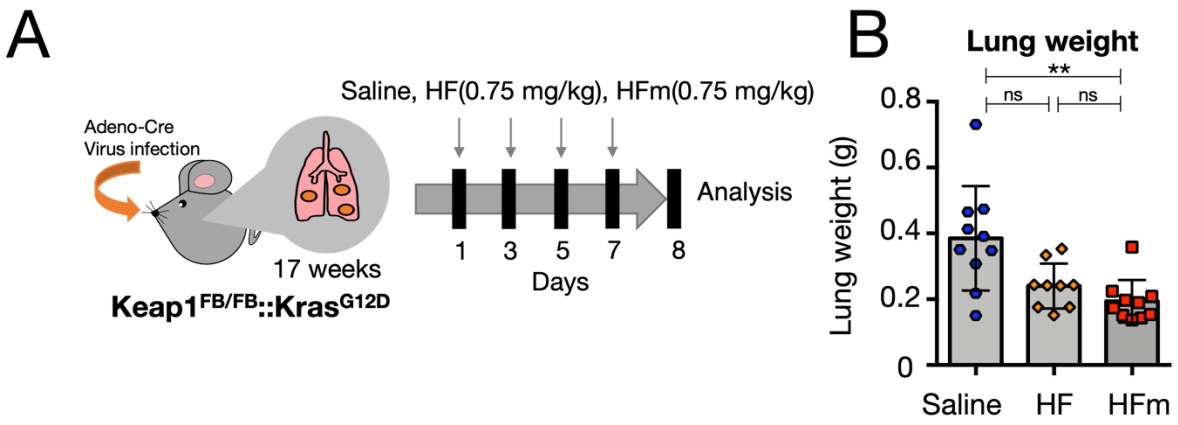

Fig. 13. HF/HFm administration suppressed Nrf2-activated tumor. (A) Experimental strategy to determine the tumor inhibitory effects of HF and HFm. Keap1$^{FB/FB}$::Kras^{G12D} mice (8-12 weeks old) were administered with Adeno-Cre virus intranasally to generated Nrf2 activated lung adenocarcinoma. Tumors were allowed to grow for 17 weeks, before treatment of the mice with saline, HF or HFm every alternate day 4 times in total. (B) Lung weight of mice after saline, HF or HFm treatment; Non-parametric Kruskal-Wallis test, *P≤0.05, **P≤0.01, ***P≤0.001, ns=not significant.

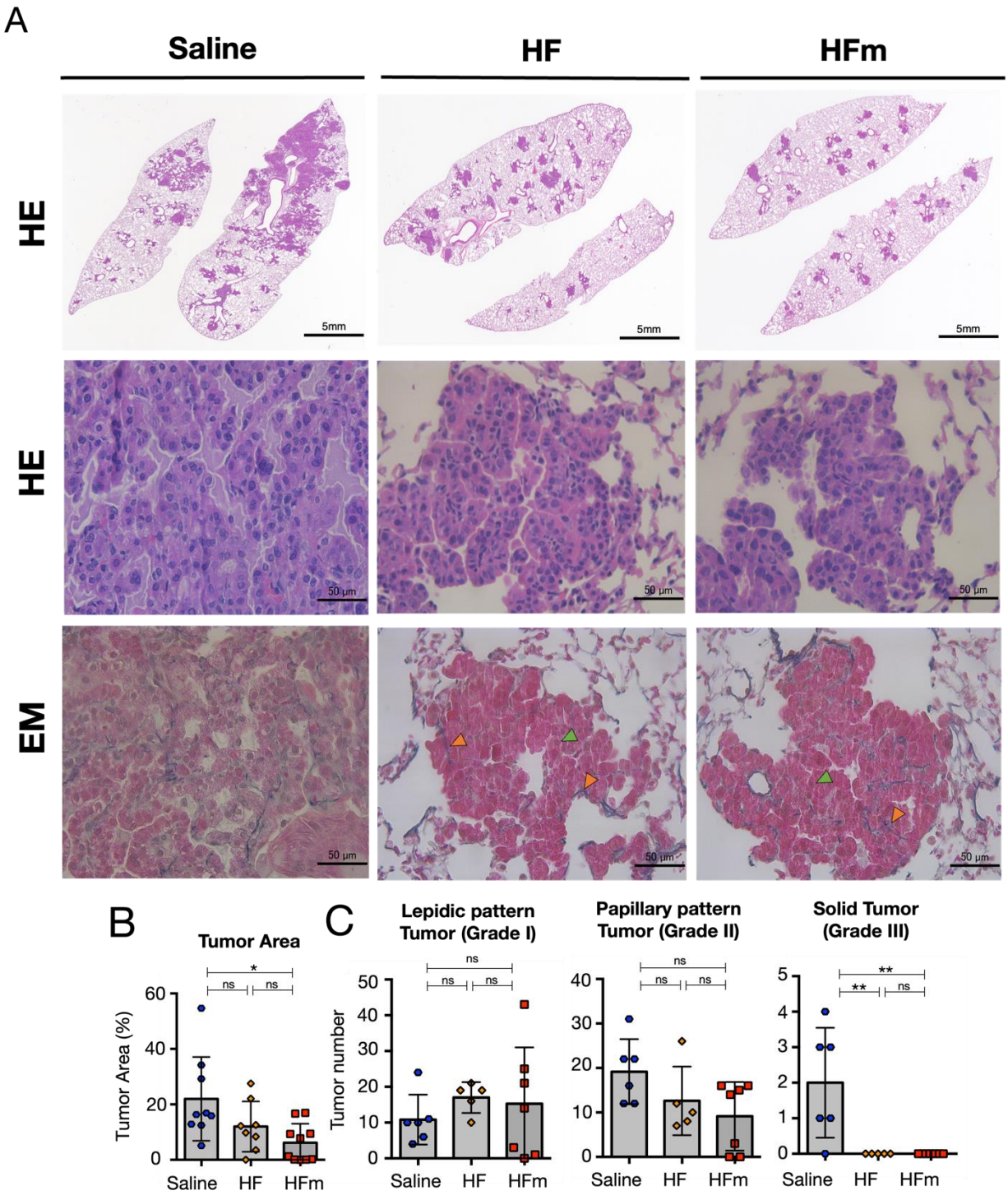
A
Saline
HF
HFm
HE
HE
EM
5mm
50 µm
B
Tumor Area
Tumor Area (%)
C
Lepidic pattern Tumor (Grade I)
Papillary pattern Tumor (Grade II)
Solid Tumor (Grade III)
Tumor number
ns
*
**
Saline
HF
HFm

Fig. 14. HF/HFm administration inhibits progression of Nrf2-activated tumor. (A) Representative lung sections stained with hematoxylin and eosin (HE) (upper and middle panels) and Elastica-Masson (lower panels) of saline, HF or HFm treated tumor bearing mice. Scale- 5mm (upper panel), 50 μm (middle and lower panel). (B) Tumor area in the saline, HF or HFm treated mice was measured using the HE stained lung cross-sections. The dark stained areas in the HE stained lung cross-sections represent the tumors; Non-parametric Kruskal-Wallis test, *P≤0.05, **P≤0.01, ***P≤0.001, ns=not significant. (C) The grade of the tumor was determined on the basis of Elastica-Masson stained lung cross-sections. Tumors in the lung consists of two types of lesions: lepidic-pattern lesions and papillary pattern lesions. If elastin is visible in the cross-section (orange arrowheads), the tumor is classified as lepidic pattern tumor (Grade I), which are assumed to be an *in-situ* growth. If such pattern is absent, and the elastin is visible as dots (green arrowheads) it is labelled as papillary patter tumor (Grade II). If the tumor is mostly composed of solid sheet and cannot be differentiated into either lepidic or papillary. it is called solid tumor (Grade III). Note that the solid tumors (Grade III) were completely absent in HF/HFm treated mice Non-parametric Kruskal-Wallis test, *P≤0.05, **P≤0.01, ***P≤0.001, ns=not significant. Graphed data are presented as means±SD.

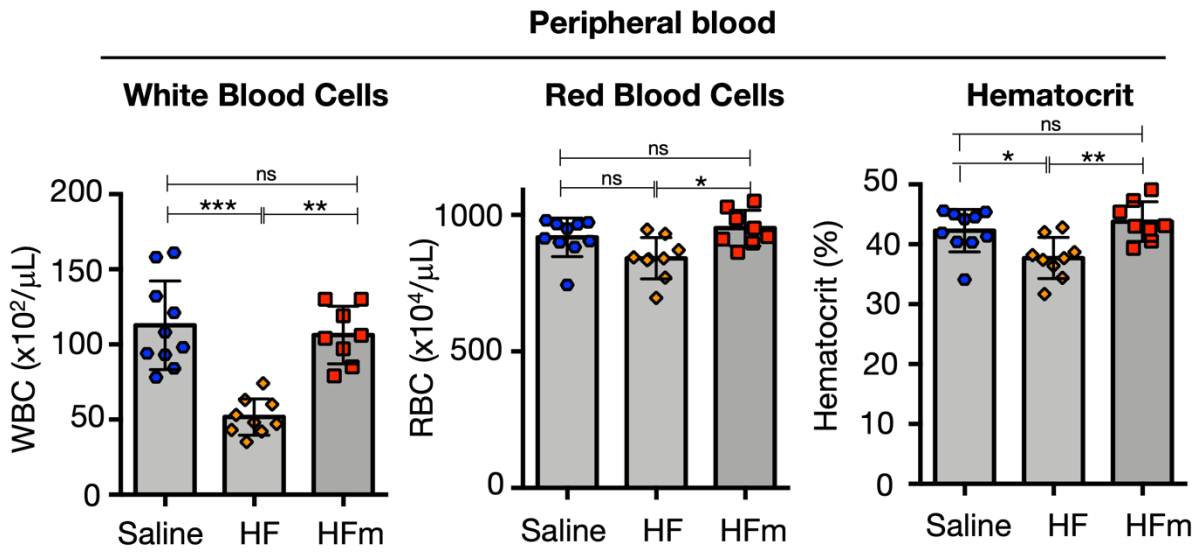

Fig. 15. HFm administration relieves leukopenia and mild anemia caused in case of HF use. White blood cell count, red blood cell count and hematocrit levels in the peripheral blood of the tumor bearing mice ($Keap1^{FB/FB}$::$Kras^{G12D}$) treated with saline, HF (0.75 mg/kg) or HFm (0.75 mg/kg); Non-parametric Kruskal-Wallis test, *P≤0.05, **P≤0.01, ***P≤0.001, ns=not significant.

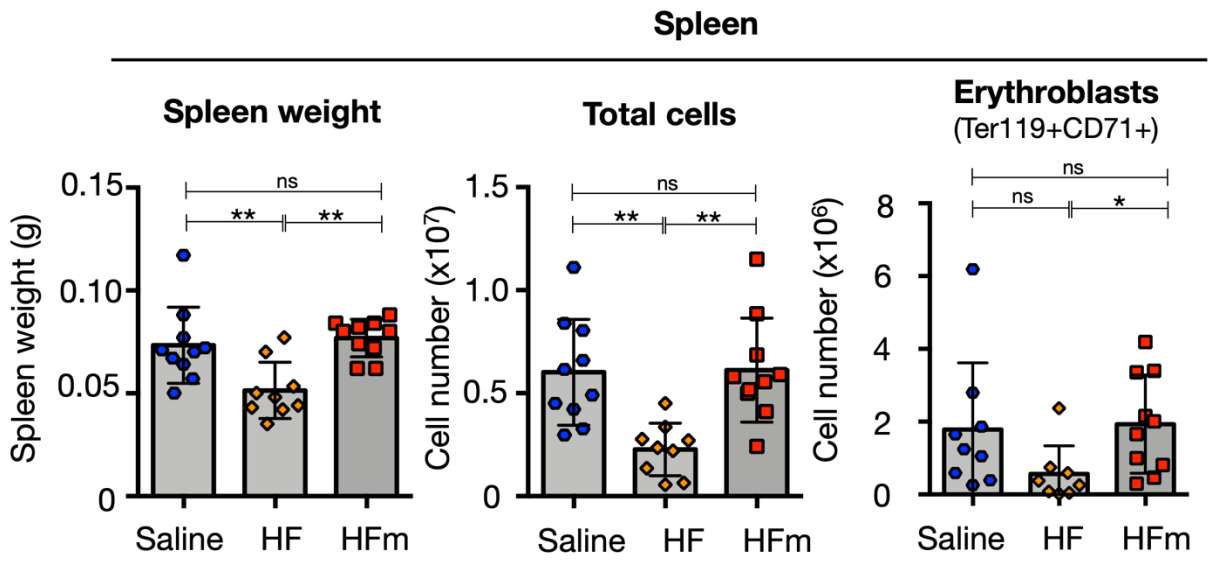

Fig. 16. HFm administration alleviates splenic atrophy and cell death of splenocytes caused in case of HF use. Spleen weight, total splenic cell count and erythroblasts (Ter119+CD71+) after saline, HF and HFm treatment. Cells were isolated from the spleen of the mice; (one-way ANOVA with Tukey's multiple comparisons test for spleen weight, Non-parametric Kruskal-Wallis test for total splenic cell count and erythroblasts)., *P≤0.05, **P≤0.01, ***P≤0.001 ns=not significant.

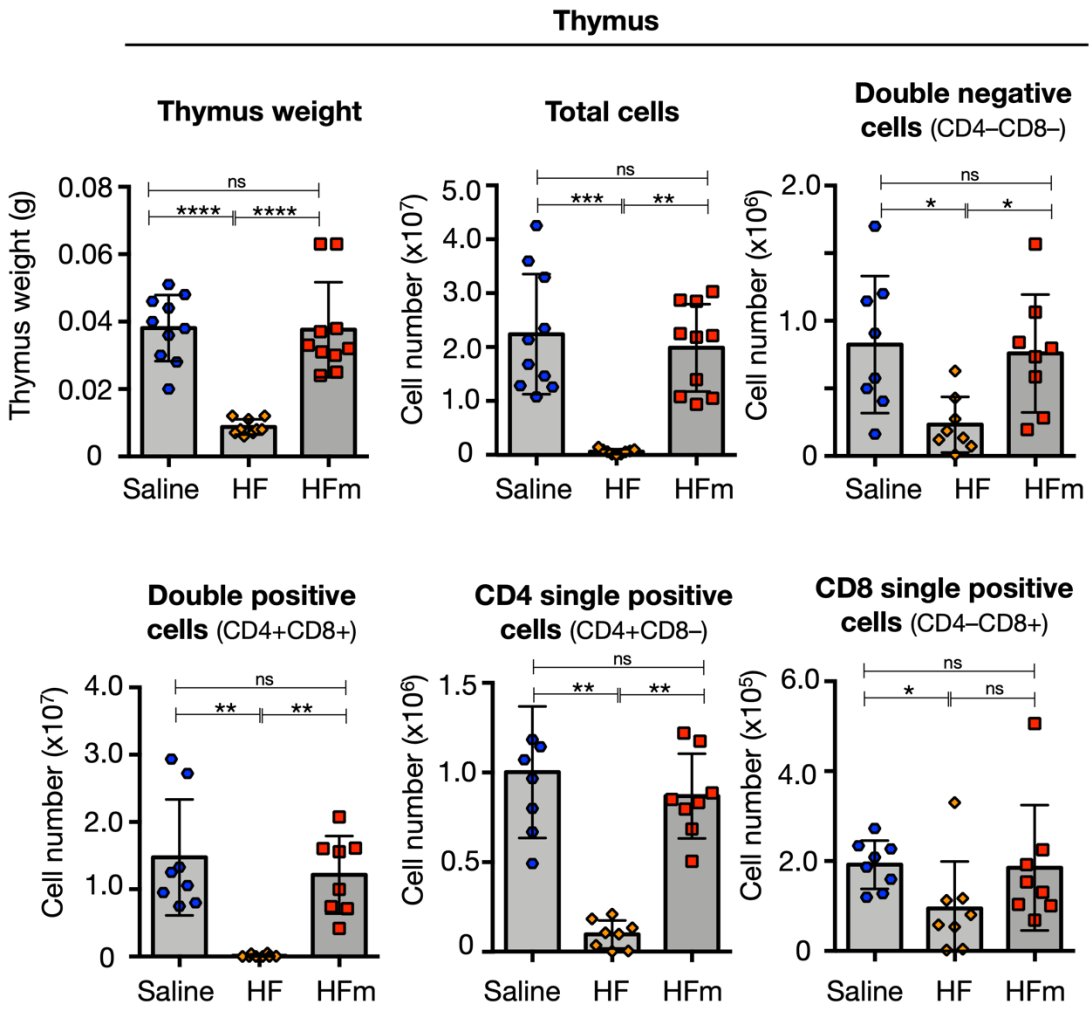

Fig. 17. HFm reduces systemic immunosuppressive side effects. Thymus weight, total thymic cells, double negative cells (CD4–CD8–), double positive cells (CD4+CD8+), CD4 single positive (CD4+CD8–) and CD8 single positive (CD4–CD8+) cells after the saline, HF and HFm treatment. Cells were isolated from the thymus; (one-way ANOVA with Tukey's multiple comparisons test for thymus weight, *P≤0.05, **P≤0.01, ***P≤0.001, ns=not significant.

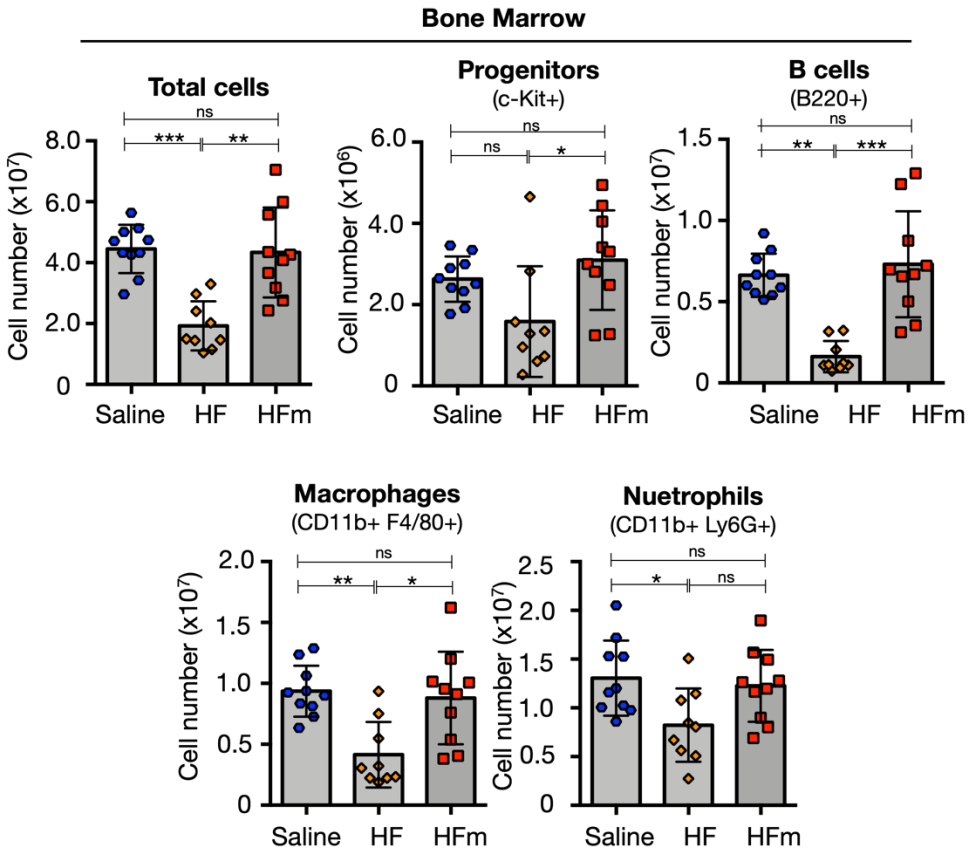

Fig. 18. HFm reduces systemic immunosuppressive side effects. Total cells, progenitor cells (c-Kit+), B cells (B220+), macrophages (CD11b+ F4/80+) and neutrophils (CD11b+ Ly6G+) isolated from saline, HF or HFm treated tumor bearing mice ($Keap1^{FB/FB}$::$Kras^{G12D}$). HF treatment resulted in severe depletion of hematopoietic and immune cells. This cell death was rescued in case of HFm use. Non-parametric Kruskal-Wallis test, *P≤0.05, **P≤0.01, ***P≤0.001,ns=not significant. Graphed data are presented as means±SD.

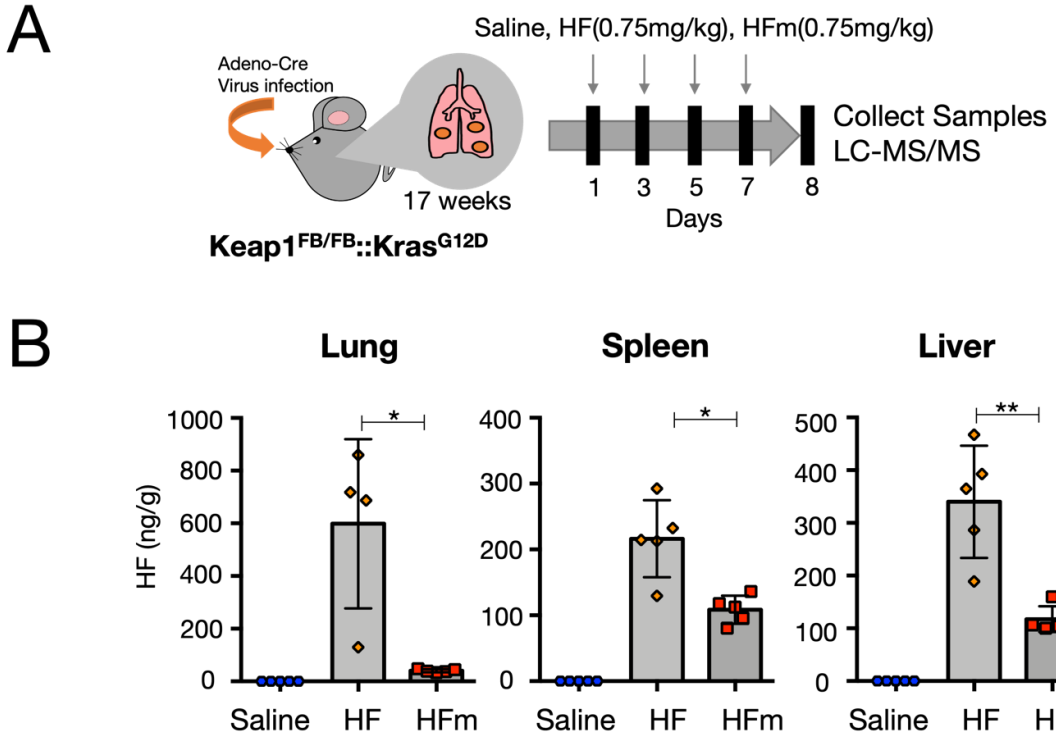

Fig. 19. HFm administration leads to lower HF accumulation in non-tumorous tissues. (A) Schematic diagram of the protocol followed for the LC-MS/MS analysis of different organs of tumor bearing mice (Keap1$^{FB/FB}$::Kras^{G12D}). The tumor bearing mice were treated with saline, HF (0.75 mg/kg) or HFm (0.75 mg/kg) every alternate day for a total of four inoculations. The samples were collected on the 8th day. (B) HF levels in lung, spleen and liver samples of the tumor bearing mice after treatment with saline, HF (0.75 mg/kg) or HFm (0.75 mg/kg). The HF accumulation in case of HFm administration was significantly less than free HF treatment. Non-parametric Kruskal-Wallis test, *P≤0.05, **P≤0.01, ***P≤0.001, ns=not significant. Graphed data are presented as means±SD.

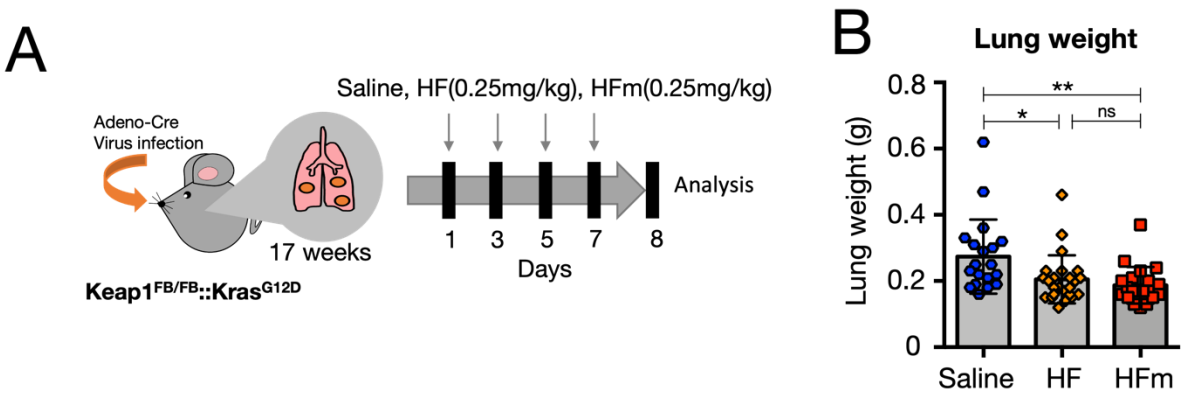

Fig. 20. HF and HFm therapies with low dose suppress Nrf2 activated tumor. (A) The treatment protocol followed during the experiment. The Keap1$^{FB/FB}$::Kras^{G12D} mice (8-12 weeks old) were treated with Adeno-Cre virus intranasally after which the tumor was allowed to grow for 17weeks. The mice were then treated with saline, HF (0.25 mg/kg) or HFm (0.25 mg/kg) every alternate day for a total of 4 times. (B) Lung weight of mice after saline, HF or HFm treatment; Non-parametric Kruskal-Wallis test, *P≤0.05, **P≤0.01, ***P≤0.001, ns=not significant.

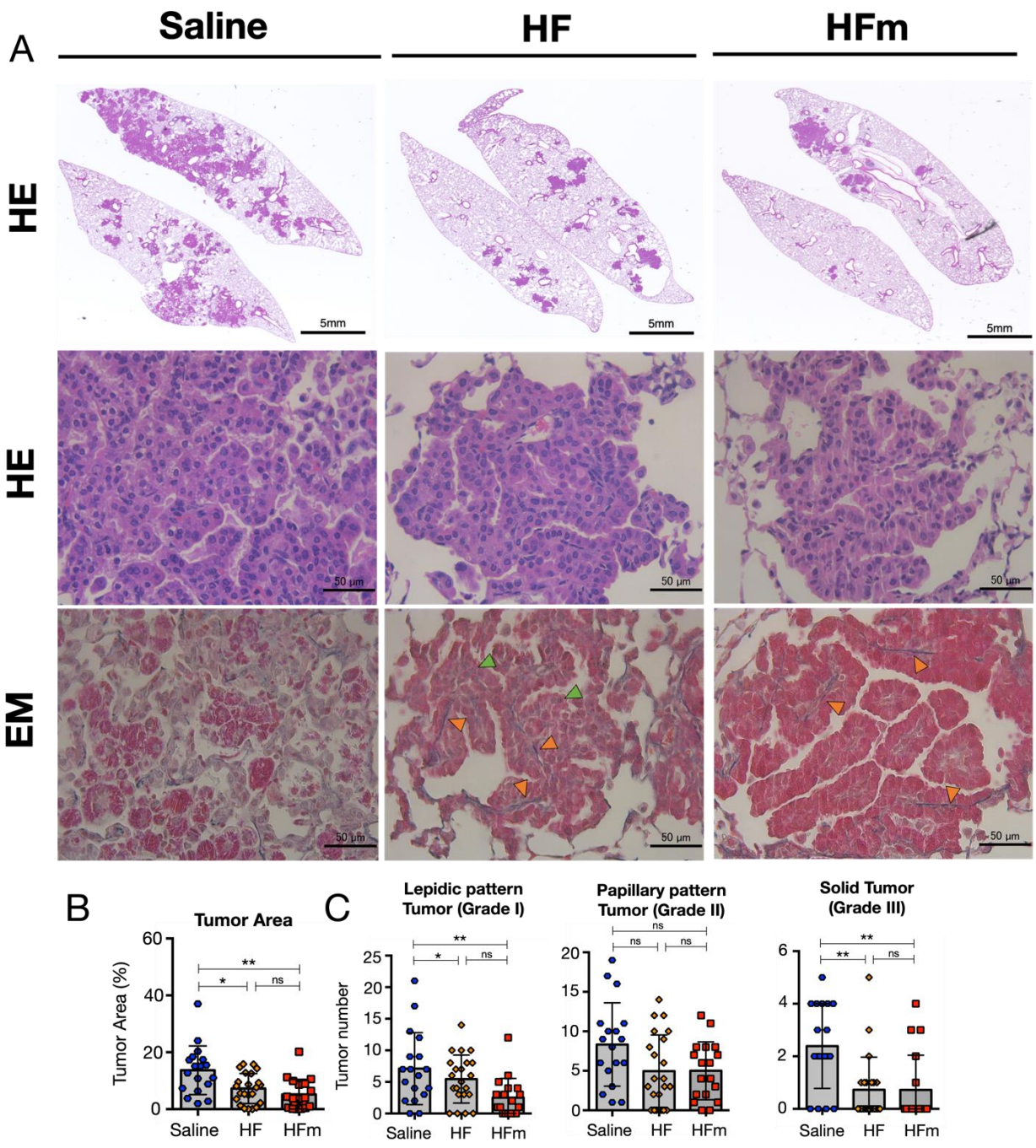
A
Saline
HF
HFm
HE
HE
EM
5mm
50 µm
B
Tumor Area
Tumor Area (%)
60
40
20
0
**
*
ns
Saline
HF
HFm
C
Lepidic pattern
Tumor (Grade I)
Papillary pattern
Tumor (Grade II)
Solid Tumor
(Grade III)
Tumor number
25
20
15
10
5
0
6
4
2
ns

Fig. 21. HF and HFm therapies with low dose eradicates Nrf2 activated tumor. (A) Representative lung sections stained with hematoxylin and eosin (HE) (upper and middle panels) and Elastica-Masson (lower panels) of saline, HF or HFm treated tumor bearing mice. Scale- 5mm (upper panel), 50 μm (middle and lower panel) (B) Tumor area in the saline, HF or HFm treated mice was measured from the HE stained lung cross-sections. The dark stained areas in the HE stained lung cross-sections represent the tumors; Non-parametric Kruskal-Wallis test, *P≤0.05, **P≤0.01, ***P≤0.001, ns=not significant. (C) The grade of the tumor was determined on the basis of Elastica-Masson stained lung cross-sections. The HF and HFm treated mice show significantly lower number of lepidic pattern tumor (Grade I) and solid tumors (Grade III) compared to the mice in the saline-treated group; Non-parametric Kruskal-Wallis test, *P≤0.05, **P≤0.01, ***P≤0.001, ns=not significant. The solid tumors did not disappear completely as is the case for high dose HF or HFm treatment.

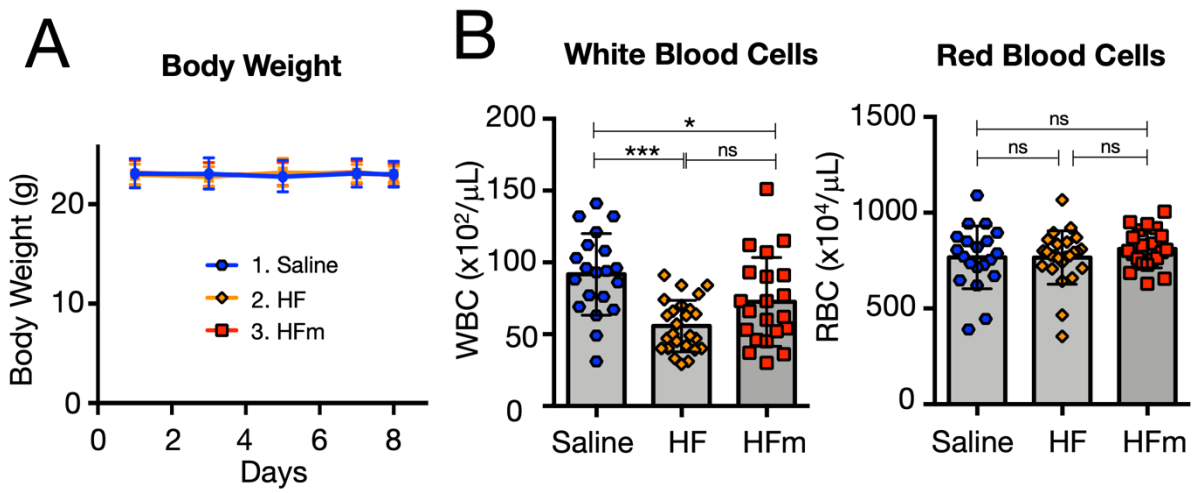

Fig. 22. HFm inoculation ameliorates leukopenia caused in the case of HF use. (A) The body weight was observed every alternate day and remained comparable in all three groups. (B) The white blood cell and red blood cells in the peripheral blood of the saline, HF or HFm treated mice. Note that HF treated mice show severe leukopenia, but the adverse effect is not seen in the case of HFm inoculations; Non-parametric Kruskal-Wallis test, *P≤0.05, ***P≤0.001 ns=not significant. Graphed data are presented as means±SD.

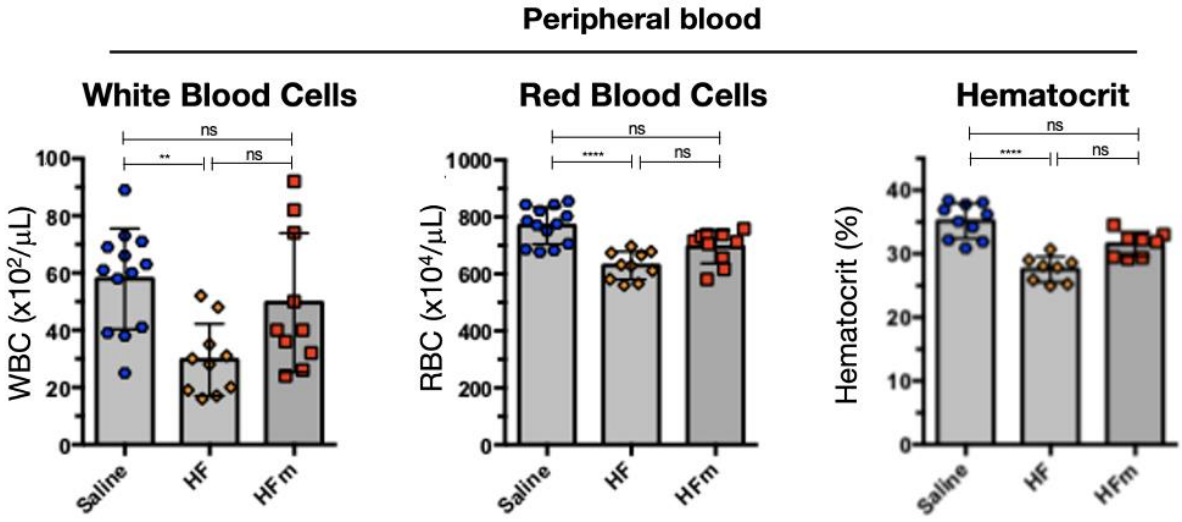

Fig. 23. High dose (0.8mg/kg) HFm treatment did not cause any adverse effect in WT mice. There was no apparent change in white blood cell, red blood cell and hematocrit levels on 0.8mg/kg HFm treatment in WT mice. HF at this dose (0.8mg/kg) on the other hand caused significant decrease in all these parameters.; Non-parametric Kruskal-Wallis test, *P≤0.05, ***P≤0.001 ns=not significant. Graphed data are presented as means±SD.

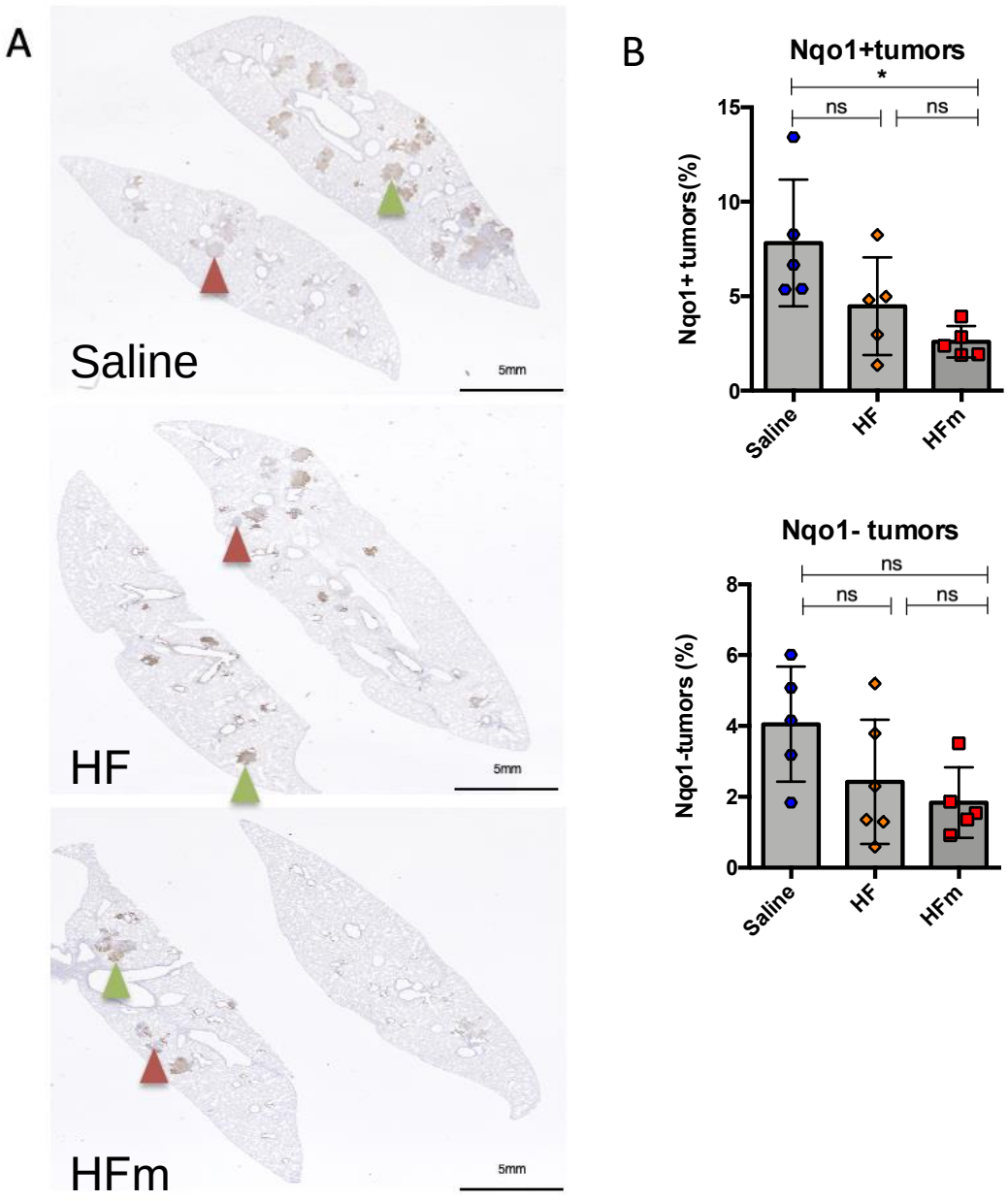

Fig. 24. HF/HFm (0.25mg/kg) treated tumor bearing mice showed decreasing trend of both Nqo1-positive and Nqo1-negative tumors. (A) Representative images of Nqo1 immunohistochemistry lung cross sections of Saline, HF and HFm treated mice showing Nqo1-positive (green arrowheads) and Nqo1-negative (red arrowheads) cancer cells. Interestingly HF/HFm treatment led to decrease in both Nqo1+ and Nqo1- tumors. (B) Graphical representation of Nqo1+ and Nqo1- tumors (%) in Saline, HF and HFm treated mice.; Non-parametric Kruskal-Wallis test, *P≤0.05, ***P≤0.001 ns=not significant. Graphed data are presented as means±SD.

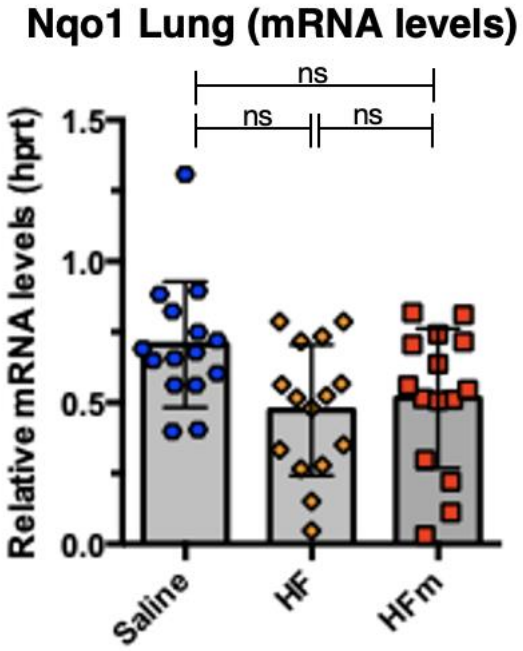

Fig. 25. Decreasing trend of Nqo1 mRNA levels were observed in the lungs of HF and HFm (0.25mg/kg) treated mice. mRNA level of Nqo1 showed a decreasing trend on HF/HFm treatment in tumor bearing mice.; Non-parametric Kruskal-Wallis test, *P≤0.05, ***P≤0.001 ns=not significant. Graphed data are presented as means±SD.

Table 1. FACS antibodies used in the current research.

Epitope	Conjugate	Clone	Company
c-Kit	APC-eFluor 780	2B8	Invitrogen
B220	BV421	RA2-6B2	Biolegend
F4/80	PE	BM8	Biolegend
Ly6G	FITC	1A8	Biolegend
CD11b	BV510	M1/70	Biolegend
CD71	FITC	R17217	eBiosciences
Ter119	PE	TER-119	eBiosciences
CD4	PE-Cy7	GK1.5	Invitrogen
CD8	APC	S3-6.7	Biolegend

Table 2. Genotyping primers used in the current research.

PRIMERS for genotyping	
KEAP1	
KEAP1 Neo 13R	GAG TCA CCG TAA GCC TGG TC
KEAP1 Neo ex 3F	CTC CGC AGA ATG TTA CTA TCCA
KRAS	
KRAS5 UNIVERSAL	CCT TTA CAA GCG CAC GCA GAC TGT AGA
KRAS MUTANT	AGC TAG CCA CAA TGG CTT GAG TAA GTC TGC A
KRAS WILDTYPE	GTC GAC AAG CTC ATG CGG GTG

Table 3. Primers and Probes for RT-qPCR.

	Forward Primer	Reverse Primer	Probe
Primers and probes for RT-PCR using Taqman probe			
rRNA	CGGCTACCACATCCAAGGAA	GCTGGAATTACCGCGGCT	TGCTGGCACCAGACTTGCCCTC
Nqo1	AGCTGGAAGCTGCAGACCTG	CCTTTCAGAATGGCTGGCA	ATTTCAGTTCCCATTGCAGTGGTTTGGG

Acknowledgement

First and foremost, I would like to express my sincere gratitude to my research advisor, Prof. Yamamoto Masayuki for his valuable and constructive suggestions during the planning and development of this research work.

I am profoundly grateful to my supervisor Dr. Suzuki Mikiko, for her enthusiastic encouragement, useful critiques, and patient guidance. My heartfelt thanks are also extended to all the members of Medical Biochemistry and related laboratories who gave me invaluable help throughout my study.

Lastly, special thanks are due to my parents Prof. Nabin Panda, Nirmala Panda and my fiancé Radhika Mishra, for their constant motivation and emotional support.